JGR Solid Earth

RESEARCH ARTICLE
10.1029/2022JB025610

Key Points:
- Heterogenous heating rates cause piles to destabilize more rapidly than homogeneous heating rates
- A narrow range of buoyancy numbers allows piles to persist to present day without being destroyed or forming a layer
- Faster mantle processing rates can replenish piles more efficiently, increasing their longevity

Supporting Information:
Supporting Information may be found in the online version of this article.

Correspondence to:
J. Panton,
pantonjc@cardiff.ac.uk

Citation:
Panton, J., Davies, J. H., & Myhill, R. (2023). The stability of dense oceanic crust near the core-mantle boundary. *Journal of Geophysical Research: Solid Earth*, *128*, e2022JB025610. https://doi.org/10.1029/2022JB025610

Received 13 SEP 2022
Accepted 26 JAN 2023

Author Contributions:
Conceptualization: James Panton, J. Huw Davies
Data curation: James Panton
Formal analysis: James Panton
Funding acquisition: J. Huw Davies
Investigation: James Panton
Methodology: James Panton, Robert Myhill
Project Administration: J. Huw Davies
Resources: J. Huw Davies
Software: James Panton, Robert Myhill
Supervision: J. Huw Davies
Validation: James Panton, J. Huw Davies
Visualization: James Panton
Writing – original draft: James Panton
Writing – review & editing: James Panton, J. Huw Davies, Robert Myhill

© 2023. The Authors.
This is an open access article under the terms of the Creative Commons Attribution License, which permits use, distribution and reproduction in any medium, provided the original work is properly cited.

The Stability of Dense Oceanic Crust Near the Core-Mantle Boundary

James Panton[1], J. Huw Davies[1], and Robert Myhill[2]

[1]School of Earth and Environmental Sciences, Cardiff University, Cardiff, UK, [2]School of Earth Sciences, University of Bristol, Bristol, UK

Abstract The large low-shear-velocity provinces (LLSVPs) are thought to be thermo-chemical in nature, with recycled oceanic crust (OC) being a contender for the source of the chemical heterogeneity. The melting process which forms OC concentrates heat producing elements (HPEs) within it which, over time, may cause any collected piles of OC to destabilize, limiting their suitability to explain LLSVPs. Despite this, most geodynamic studies which include recycling of OC consider only homogeneous heating rates. We perform a suite of spherical, three-dimensional mantle convection simulations to investigate how buoyancy number, geochemical model and heating model affects the ability of recycled OC to accumulate at the core-mantle boundary. Our results agree with others that only a narrow range of buoyancy numbers allow OC to form piles in the lower mantle which remain stable to present day. We demonstrate that heterogeneous radiogenic heating causes piles to destabilize more readily, reducing present day CMB coverage from 63% to 47%. Consequently, the choice of geochemical model can influence pile formation. Geochemical models which lead to high internal heating rates can cause more rapid replenishment of piles, increasing their longevity. Where piles do remain to present day, first order comparisons suggest that old (hot) OC material can produce seismic characteristics, such as Vs anomalies, similar to those of LLSVPs. Given the range of current density estimates for lower mantle mineral phases, subducted OC remains a contender for the chemical component of thermo-chemical LLSVPs.

Plain Language Summary Large, pile-like structures at the base of Earth's mantle may be partially composed of accumulations of recycled oceanic crust. When oceanic crust is formed, heat producing elements are concentrated within it. This causes oceanic crust to experience relatively high heating rates compared to surrounding material when it is recycled into the mantle. A consequence of the high heating rates is that piles of oceanic crust may become unstable and so may not survive to present day. We conduct three-dimensional numerical mantle simulations to investigate how the excess chemical density of recycled oceanic crust affects the survival of piles. In line with previous work, we find only a narrow range of excess chemical densities allow the survival of piles to the present day. Piles are more readily destroyed when internal heating is controlled by the concentration of heat producing elements compared to when internal heating is distributed evenly through the mantle. Consequently, assumptions made in the geochemical model, which controls the distribution of heat producing elements, can affect the long-term stability of piles.

1. Introduction

Seismic tomography models have discerned the presence of two mantle structures close to the core-mantle interface characterized by low seismic velocities. These large low-shear velocity provinces (LLSVPs) sit beneath Africa and the Pacific plate and exhibit a shear velocity anomaly of $\delta lnV_s \approx -2\%$. Spatially, they are both voluminous and broad (Cottaar & Lekić, 2016), with seismic tomography models showing high power in spherical harmonic degree 2 and to a lesser extent degree 3 structures (Koelemeijer et al., 2016; Ritsema et al., 2011) in the lower mantle. These structures exist within and above the D" layer and may extend >1,000 km into the mantle from the core-mantle boundary (CMB) (He & Wen, 2009; Lekic et al., 2012), with the African LLSVP being significantly taller than the Pacific LLSVP (Ni et al., 2002; Yuan & Li, 2022). Mantle plumes are claimed to cluster around their edges (Thorne et al., 2004) potentially entraining material to be sampled by melting beneath ocean islands. Despite the morphology of LLSVPs being well constrained, increasingly accurate measurements of their material properties and possible direct links to the surface via plumes, their origin and composition remain a matter of debate. This is because the very characteristics that define LLSVPs have a non-unique source; the velocity anomaly may originate thermally, chemically, or thermo-chemically. Consequently there are competing theories over the nature of LLSVPs, are they of a predominantly thermal origin (D. R. Davies et al., 2015;

Schubert et al., 2004), or thermochemical in nature (Deschamps & Trampert, 2003; Karato & Karki, 2001; Nakagawa & Tackley, 2014)?

The argument for a thermochemical origin is generally split into two possible scenarios. The first is that LLSVPs are composed of dense primordial material (Deschamps et al., 2011; Garnero & McNamara, 2008; Labrosse et al., 2007; M. Li & McNamara, 2018) and the second is that they formed from the accumulation of recycled oceanic crust (henceforth referred to as OC) (Christensen & Hofmann, 1994; Coltice & Ricard, 1999; Tackley, 2011). A third scenario arises from this, where LLSVPs may comprise heterogeneity from both recycled OC and primordial material, a so-called basal melange (Gülcher et al., 2021; Jones et al., 2021; Tackley, 2012).

In the past, many lines of evidence appeared to support the thermochemical explanation of LLSVPs, including the apparent sharp sides of the African LLSVP (Ni et al., 2002) and an elevated ratio between shear and compressional wavespeed (Masters et al., 2000; Romanowicz, 2001). Numerical geodynamic modeling by D. R. Davies et al. (2012) showed that sharp sides and low shear wave anomalies could be explained by a purely thermal case. Further, the high S/P wavespeed ratio could also indicate the presence of post-bridgmanite (Koelemeijer et al., 2018). Nonetheless, there are still strong arguments for a thermo-chemical origin. Given the prevalence of mantle plumes originating from the edges and within LLSVPs, high $^{3}He/^{4}He$ measured in many ocean island basalts (OIBs) is given as evidence for a primordial origin of thermochemical LLSVPs. This end-member has received significant attention by the modeling community (Deschamps et al., 2012; Y. Li et al., 2014; Williams et al., 2015), and recently has been scrutinized for the effect that high internal heating rates has on the stability of such piles (Citron et al., 2020).

The second end-member is supported by the observation of subducted OC entering the lower mantle in seismic tomography (Grand et al., 1997). Additionally, many mantle plumes contain a component of OC (Kokfelt et al., 2006; Sobolev et al., 2000; X.-J. Wang et al., 2018). Christensen and Hofmann (1994) showed that long term segregation of OC into the lower mantle could result in accumulations forming into pile like structures. This requires subducted basalt to have an excess density compared to ambient mantle material, which has been determined by mineral physics experiments to be 0.5%–5% denser in the lower mantle (Hirose et al., 2005; Ricolleau et al., 2010; Ringwood & Irifune, 1988; W. Wang et al., 2020). Simulations by Brandenburg et al. (2008) and Jones et al. (2020) suggest that subducted OC is required to have an excess density of at least +3% relative to ambient mantle compositions in order for significant volumes to be retained at the CMB. Other numerical experiments agree that the lower mantle becomes enriched in OC if the OC is chemically dense (Ogawa, 2003, 2007) and this can lead to large piles of compositionally distinct material developing (G. F. Davies, 2002; Huang et al., 2020; Xie & Tackley, 2004). However, the majority of studies to date which include recycling of OC material have been conducted in 2D geometry which cannot account for the full complexity of the flows which shape such piles. The partial melting process that forms OC concentrates heat producing elements (HPEs) such as U, Th, and K, giving recycled crust a strong potential to heat up relative to the surrounding, relatively HPE depleted, mantle. Despite this, almost all studies to date in which OC is recycled into the mantle (with just a small number of exceptions, e.g., Ogawa, 2014; Xie & Tackley, 2004) have opted for a homogeneous heating rate throughout the mantle, which is often constant over time. For this reason, the effect that relatively high heating rates within piles has on their formation and evolution is poorly known.

In this study we test the hypothesis that LLSVPs are composed of recycled OC material which is enriched in HPEs using 3D spherical models. Our models are heated internally by the decay of HPEs, which are concentrated into basaltic OC by a self consistent melting regime. We vary the excess density of the OC compared to ambient mantle compositions by varying the buoyancy number (B) of our simulations in order to assess how easy or difficult it is to form piles in the D" layer. We also test different chemical models to vary the distribution and concentration of HPEs in the model to assess the impact this has on pile formation and retention. In our analysis we examine the age and morphology of accumulations of subducted OC and in a case where piles persist to present day we present predictions of the seismic velocity for first order comparisons against observations.

2. Methods

2.1. Dynamic Model

In this study we use the three-dimensional mantle convection code, TERRA (Baumgardner, 1985; Bunge et al., 1997; D. R. Davies et al., 2013) to solve the governing equations for mantle convection under the Boussinesq

Table 1
Common Parameters to All Simulations and Their Values

Symbol	Parameter	Value	Unit
Ts	Surface temperature	300	K
T_{cmb}	CMB temperature	3,000	K
η_0	Reference viscosity	5×10^{21}	Pas
ρ_0	Reference density	4,500	kgm^{-3}
k	Thermal conductivity	4	$Wm^{-1}K^{-1}$
α	Thermal expansivity	2.5×10^{-5}	K^{-1}
C_p	Specific heat capacity	1,100	$Jkg^{-1}K^{-1}$

Note. Reference viscosity is equal to the viscosity of the upper mantle.

approximation and assuming incompressibility (McKenzie et al., 1974). Values for common parameters can be found in Table 1. A regular icosahedron projected onto a sphere provides the basis of the grid structure at each of the 65 radial layers (average radial spacing of 45 km). The grid is further discretized identically at each radial layer to give an average lateral grid spacing of ~33 km at the CMB and ~60 km at the surface, with a total of >10 million grid points. Both the top and bottom boundaries are free-slip and iso-thermal at 300 and 3000 K respectively. Our calculations are freely evolving mantle convection simulations which lack true plate tectonics. To this end we employ a partially strong lithosphere via a depth dependent viscosity in order to strike a balance between the surface velocity and surface heat flux. Our viscosity profile also contains a ×30 jump at 660 km (Hager et al., 1985, van Keken & Ballentine, 1998) and a drop near the CMB to approximate lower viscosities induced by the thermal boundary layer and the exothermic bridgmanite phase transition in the lowermost mantle (Y. Li et al., 2014).

2.2. Particles

Active particles are used to track chemical information throughout the mantle. Each of the $\sim 1.1 \times 10^8$ particles stores its mass, bulk composition (C) and abundance of certain isotopes. The bulk composition may vary between 0 and 1, where C = 0 is completely depleted (harzburgitic), C = 1 is completed enriched (basaltic) and we assume the average mantle composition to be $C_{av} = 0.25$, which we denote as lherzolite. We refer to the end-member compositions with the terms "harzburgite," "basalt" and "lherzolite" for simplicity, despite these having petrological implications which we do not include in our models. Simulations are initialized with 1/2 of all particles having a composition C = 0.25, 1/8 with C = 1 and 3/8 with C = 0, uniformly distributed throughout the mantle giving an average mantle composition of C = 0.25. The bulk composition and depth of particles affects the local density. In the upper mantle (<660 km depth) completely enriched particles are 3% denser than completely depleted particles (Ono et al., 2001) and we vary the excess density of basaltic material in the lower mantle (>750 km depth). Due to OC being relatively cool compared to ambient mantle, there is a delayed transition to dense lower-mantle mineral phases within subducted slabs from 660 to 750 km depth (Irifune & Ringwood, 1993). This is modeled by making basalt 3.75% more buoyant than material of average mantle composition within this depth range (G. F. Davies, 2008). Our model includes a simplified parameterization for the olivine system phase transitions 410 and 660 km depth (Table 2). We note that this implementation is not composition dependent but nonetheless allows us to capture some of the behaviors that are associated with these phase transitions (Price et al., 2019; Wolstencroft & Davies, 2011). Melting in the models is controlled by a simple linear solidus, dependent on depth (z) and bulk composition (Price et al., 2019; van Heck et al., 2016):

$$T_{\text{solidus,dry}}(z, C) = T_{\text{meltsurf}} + zT_{\text{meltslope}} + (1 - C)T_{\text{meltcomp}} \quad (1)$$

where $T_{\text{meltsurf}} = 1400$ K is the melting temperature of $C = 1$ material at the surface, $T_{\text{meltslope}} = 2.5$ K km^{-1} is the gradient of the solidus, and $T_{\text{meltcomp}} = 500$ K is the temperature difference between the solidi of $C = 0$ and $C = 1$ material. Temperature is linearly interpolated from the grid to each particle in order to determine whether melting may occur. During melting a particle's bulk composition is reduced so it becomes more depleted. The new composition of a melting particle is therefore defined by a particle's temperature and depth on the solidus ($C_{\text{new}} = C(T, d)$). Note that a particle may not be depleted beyond $C = 0$, at which point the composition is assumed to be so refractory that it cannot experience further melting. The amount of melt produced (M_m) is calculated by multiplying the mass of the melting particle (M_s) by the degree of melting ($F = C_{\text{old}} - C_{\text{new}}$), as described in van Heck et al. (2016) and the melt is always of composition $C = 1$.

Table 2
Olivine Phase Change Parameters for an Assumed Composition With 67% Olivine

Depth (km)	$\Delta\rho$ kg m^{-3}	Clapeyron slope MPa K^{-1}
410	230	2.25
660	380	−1.5

Note. Density difference relative to PREM (Dziewonski & Anderson, 1981).

Particles store abundances of the radioactive isotopes ^{235}U, ^{238}U, ^{232}Th and ^{40}K, as well as their stable daughter isotopes (^{207}Pb, ^{206}Pb, ^{208}Pb and ^{40}Ar respectively and ^{4}He), the non-radiogenic isotopes ^{204}Pb, ^{36}Ar and ^{3}He and also water. Decay constants for each radioactive isotope (Table 3) control their rate of decay. For the purposes of this study we are most interested in

10.1029/2022JB025610

Table 3
Isotope Information

Isotope	Initial concentration (mol g^{-1})	Decay constant (s^{-1})	Decay energy (MeV)	Partition coefficient
^{235}U	2.11×10^{-11}	9.85×10^{-10}	46.40	0.007
^{238}U	1.47×10^{-10}	1.55×10^{-10}	51.70	0.007
^{232}Th	3.91×10^{-10}	4.95×10^{-11}	42.66	0.008
^{40}K	6.14×10^{-09}	5.54×10^{-10}	1.34	0.010

Note. Initial concentrations are given at 3.6 Ga before any material has been extracted to the continental reservoir.

the radioactive isotopes as the energy released during their decay is used to internally heat the mantle heterogeneously (see Table 3 for decay energy). We initialize trace element abundances from 3.6 Ga in order to prevent having to model early Earth conditions, when high temperatures may have lead to extremely low mantle viscosities. During melting, trace elements are depleted from the melting particle according to the batch melting equation

$$A_l = F\left(\frac{A_0}{F + (D_i(1 - F))}\right) \tag{2}$$

where A_0 and A_l are the number of atoms of the isotopes before melting and lost during melting respectively and D_i is an isotope's partition coefficient (Table 3). Isotopes with different partition coefficients are therefore fractionated during melting. The isotopes and bulk composition component lost from a particle during melting form a "melt packet" which is instantaneously migrated to the particle(s) closest to the surface in cells directly above the melting particle. The amount of melt that a particle may receive is equal to $(1 - C_r) \times M_r$, where C_r is the bulk composition of the receiving particle and M_r is the mass of the receiving particle. Receiving particles cannot become more enriched than $C = 1$, so melt may have to be distributed amongst multiple particles, in which case trace elements are distributed according the mass fraction of melt assigned to each particle. Handling melt distribution in this way ensures conservation of bulk composition. The melting process generates an enriched (basaltic) layer at the surface which is underlain by a depleted (harzburgitic) layer, similar to how we think of OC forming.

We also consider non-magmatic processes for fractionating trace elements. Following the method of Panton et al. (2022), ^{235}U and ^{238}U are recycled from the continental reservoir, which tracks the number of mols of isotopes that are isolated from the mantle, after 2.4 Ga. This accounts for the oxidation of U^{4+} to U^{6+} after the onset of the great-oxygenation event, allowing U to become fluid mobile and be recycled from the continents into the mantle via hydrothermal addition to OC at ridges (Andersen et al., 2015; Michard & Albarede, 1985). The continental reservoir is populated immediately after isotopes have been initialized, prior to the first convection iteration. One third of all ^{235}U, ^{238}U, ^{232}Th, and ^{40}K is removed from each particle in the mantle and added to the continental reservoir. This end-member crustal growth model implicitly assumes full continent extraction prior to 3.6 Ga (Armstrong, 1968). Relative solubility differences cause preferential removal of K from subducted slabs relative to U and Th (Lassiter, 2004; Tatsumi & Kogiso, 1997). This is accounted for by removing a fraction (10%) of the ^{40}K in each melt packet to the continental reservoir. The net effect of these fractionation processes is that particles with a more basaltic composition than average mantle become enriched in radioactive trace elements.

2.3. Seismic Properties

The next step is to compare the results of our geodynamic simulations with seismic observations of the Earth. It is not possible to uniquely invert seismic data to obtain temperature and composition, and so we instead use the pressure, temperature, and compositions from our geodynamic models to estimate seismic properties. To do this, we use the thermodynamic data set of Stixrude and Lithgow-Bertelloni (2022) as implemented in the software Perple_X (Connolly, 2009). We assign a six-oxide bulk composition to each of our "lithologies" (Table 4), and then create lookup tables for densities and perfectly elastic seismic velocities (Vp, vs.) for each of these compositions. Attenuation is accounted for using the model of Goes et al. (2004) and Maguire et al. (2016). Parameters correspond to their model Q7g, which provides good agreement with the data provided by Matas and Bukowinski (2007).

Table 4
Assumed Molar Composition of Three End Member Lithologies

	Harzburgite	Lherzolite	Basaltic OC
SiO_2	36.184	38.819	52.298
MgO	56.559	49.894	15.812
FeO	5.954	6.145	7.121
CaO	0.889	2.874	13.027
Al_2O_3	0.492	1.963	9.489
Na_2O	0.001	0.367	2.244

Particles with a model bulk composition which lies in between 0.00 and 0.25 are treated as a mechanical mixture (Xu et al., 2008) of harzburgite and lherzolite, while those with a composition of 0.25–1.00 are treated as a mechanical mixture of lherzolite and basaltic OC. The relative proportions of these endmember lithologies are interpolated to the grid so that each node can be assigned proportions of the three lithologies, in addition to pressure and temperature. The seismic properties at each node are obtained by taking

Table 5
Buoyancy Number of Each Simulation Presented in This Study and Other Treatment for Varying Distribution of HPEs

Case	Buoyancy number	Other treatment
B0.00	0.0	-
B0.22	0.22	-
B0.33	0.33	-
B0.44	0.44	-
B0.55	0.55	-
B0.66	0.66	-
B0.77	0.77	-
B0.88	0.88	-
noU	0.55	No U recycling
noCont	0.55	No continental reservoir
U2C	0.55	Continuous continent extraction
UH	0.55	Uniform heating

the harmonic mean of the velocities for each lithology, weighted according to their proportions.

Our procedure for estimating seismic velocities is therefore a postprocessing step. This allows us to vary the excess density of OC in the geodynamic simulations independent from the thermodynamic models. This is not strictly consistent but does allow us to investigate a wide parameter range without worrying about tweaking many parameters. Our output incorporates the seismic effects of reactions including the olivine to wadsleyite ("410"), ringwoodite to bridgmanite ("660") and bridgmanite to post-perovskite phase transitions, even though only the "410" and "660" transitions are accounted for in our dynamic models (Table 2).

The thermodynamic modelset used in this study lacks some features that could be seismically important in the real Earth. There is no spin transition in ferropericlase, for example, whose influence could potentially be visible for two reasons. First, seismic waves are expected to influence the proportions of high and low spin iron, lowering the bulk modulus. Second, the spin transition is expected to increase the amount of iron in lowermost mantle ferropericlase relative to cases with no transition. In addition, no reduced phases (iron, iron sulfide) are included in the data set, and all iron is assumed to be ferrous. The second order phase transition in stishovite may also reduce seismic velocities in subducted OC.

2.4. Parameter Space

The buoyancy number has consistently been shown to be important in maintaining a stable dense layer in the lowermost mantle (Deschamps & Tackley, 2009; Le Bars & Davaille, 2004; M. Li & McNamara, 2013; Oldham & Davies, 2004). In the context of our models, the buoyancy number can be translated into a maximum density difference between subducted OC and ambient mantle compositions. In order to investigate the stability of lower mantle accumulations of subducted OC which are internally heated from the decay of radioactive isotopes, we systematically vary the buoyancy number of OC in the lower mantle (see Table 5). Under certain conditions, this should allow accumulations of OC to develop self consistently, that is to say we need not prescribe a dense primordial layer. The buoyancy number is given by

$$B = \frac{\Delta \rho_{\mathrm{b}}}{\alpha_{\mathrm{s}} \rho_{\mathrm{s}} \Delta T} \tag{3}$$

where $\Delta\rho_{\mathrm{b}}$ is the intrinsic density difference between the material and an average mantle composition, α_{s} is the coefficient of thermal expansion, ρ_{s} is the mantle reference density, and ΔT is the temperature difference across the mantle. Note that the buoyancy numbers quoted in Table 5 are those of purely basaltic material. The buoyancy number for a particle with a arbitrary composition (B_c) is given by

$$B_c = B\frac{C - C_{av}}{1 - C_{av}}. \tag{4}$$

As the degree of HPE enrichment will affect the local heating rate, we also present cases to investigate the effect of different treatment of non-magmatic HPE fractionation processes and uniform radiogenic heating of the mantle. In case *noU* we form a continental reservoir prior to 3.6 Ga but do not allow U recycling into the mantle and case *noCont* does not include the formation of a continental reservoir before 3.6 Ga (i.e., there is a higher concentration of HPEs in the mantle). Case *U2C* has a reduced continental reservoir prior to 3.6 Ga (1/6 of all HPEs removed from particles instead of 1/3) but a fraction (10%) of U, Th, and K isotopes are removed from the melt to the continental reservoir to simulate continuous continent extraction. In case *UH* the radiogenic heating produced within the mantle is uniformly distributed, rather than being concentrated in HPE enriched material.

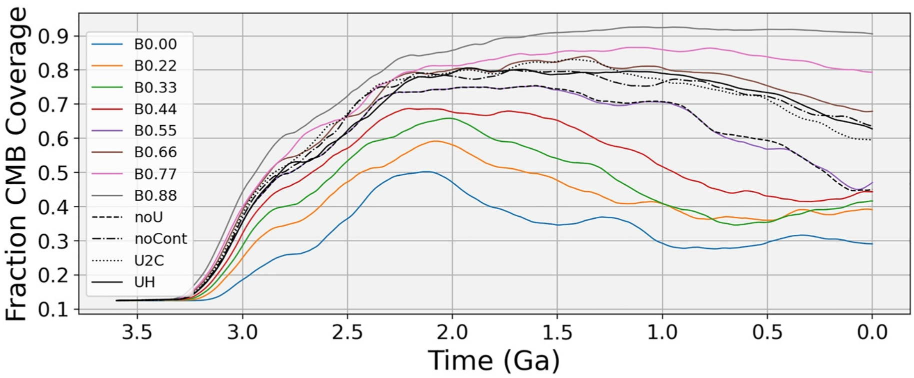

Figure 1. Fraction CMB coverage from start of calculation (3.6 Ga) to present day for different buoyancy numbers and non magmatic fractionation treatments.

3. Results

3.1. The Effects of Buoyancy Number

Visualizations show that in all cases there is an initial period of high melt productivity followed by widespread subduction of large volumes of enriched OC material (Supplementary videos V1–V8, https://doi.org/10.5281/zenodo.7544389). The amount of OC material that reaches the CMB region varies with the buoyancy number of the simulation (Figure 1), as does its subsequent rate of removal. For buoyancy numbers of ≤0.55, large volumes of enriched, basaltic material rapidly accumulate but are subsequently removed in hot upwelling regions. By the present day these accumulations have been largely eroded (Figures 2a–2d) accounting for the reduction in CMB coverage in these cases (Figure 1). In the case of *B0.55*, large volumes of basaltic material can be seen in the mid-mantle at present day, having been recently destabilized and removed from the CMB (Figure 2e). For cases *B0.77* and *B0.88* much of the recycled OC that reaches the CMB remains there to present day, forming a blanket of enriched material (Figure 2g). At these high buoyancy numbers the CMB only becomes exposed when penetrated by strong downwellings. For case *B0.66*, the accumulations of subducted OC are in a transformative state, where they have formed piles by the sweeping action of downwelling material and are beginning to be eroded by entrainment.

In Citron et al. (2020) CMB exposure is used as a measure for identifying when different convective regimes develop due to the inclusion of a primordial dense layer in their simulations. For our class of simulations, where thermochemical piles develop due the accumulation of recycled OC material, it is more appropriate to think of this as CMB coverage. We define CMB coverage as the fraction of particles in the lowermost layer with a bulk composition of C = 1. For each simulation the CMB coverage is initially 12.5% due to C = 1 material initially comprising 12.5% of all particles (Figure 1). Typically the CMB coverage stays at 12.5% for a short period of time while the recycled OC material descends from the surface to the base of the mantle. There is then a period of increasing CMB coverage as more recycled OC accumulates followed by a period of slowly decreasing CMB coverage as old recycled material is removed from the CMB whilst being buffered by newly recycled material. Two general trends are observed between cases with varying buoyancy numbers. One is that higher buoyancy numbers develop a larger maximum CMB coverage and the other is that for higher buoyancy numbers the inflection point at which CMB coverage begins to decrease is generally later on in the calculation. Only simulations in which $B > 0.55$ have more than 50% CMB coverage at present day. There is a particularly pronounced difference in the present day CMB coverage between cases *B0.55* and *B0.66*.

Radially averaged present day melting ages (average time since particles last underwent melting), show a gradual tendency toward younger ages in the lowermost mantle toward the CMB (Figure 3c). The oldest average melting ages are observed in cases with the highest buoyancy numbers. Buoyancy number does not affect the surface heat flux for the first 700 Myr of model time (Figure 3a). Thereafter is a general trend for surface heat flux to decrease with time, though the exact rates depend on the buoyancy number of the simulation. This could be considered an Earth-like behavior, as Earth's surface heat flux is thought to decrease with time (Turcotte, 1980). Earth's mantle surface heat flux is currently estimated to be ∼39 TW, assuming the continental crust accounts for ∼8 TW of the total surface heat flux J. H. Davies and Davies (2010). The present day values of mantle surface heat flux are

10.1029/2022JB025610

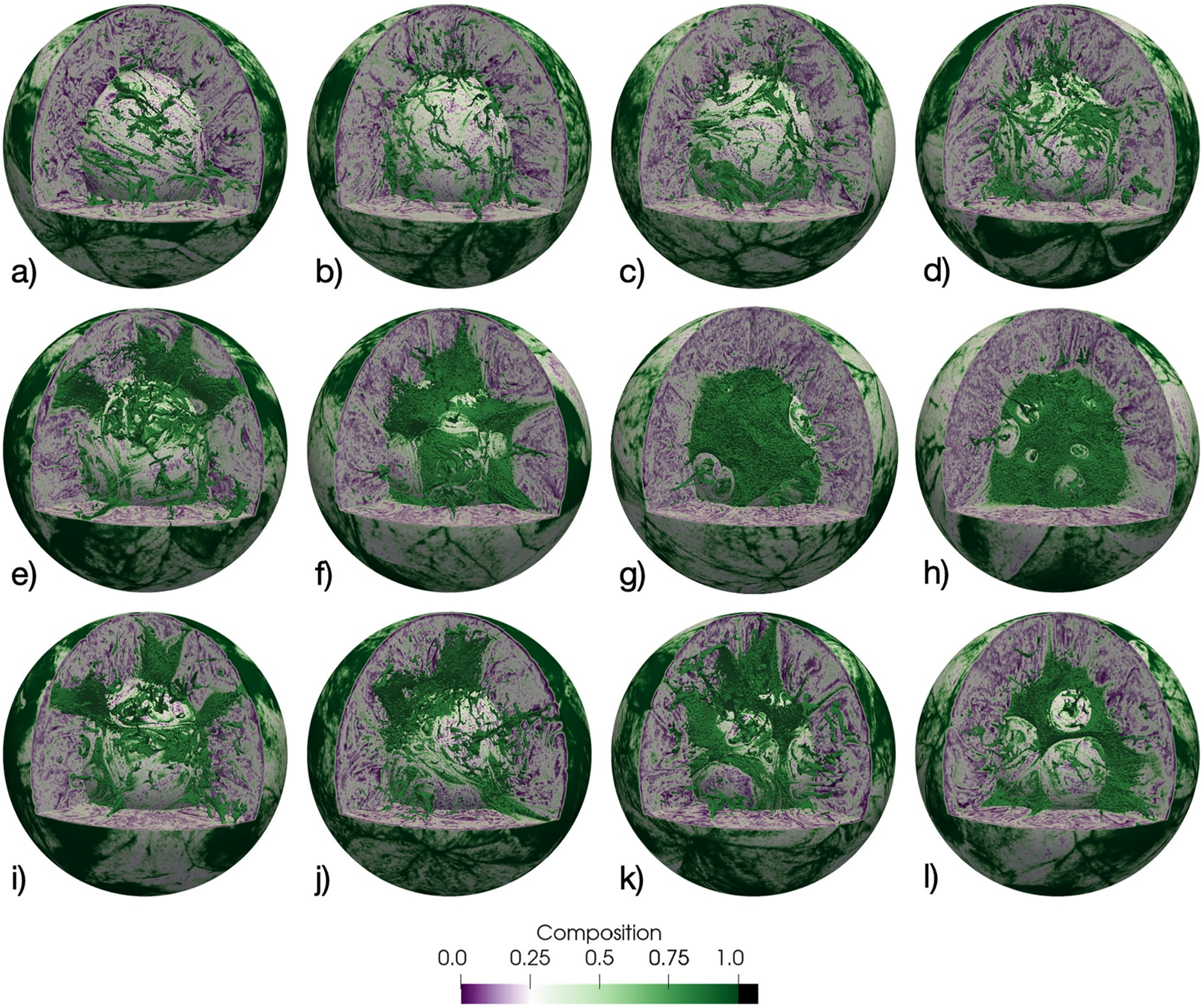

Figure 2. Visualizations of the composition field at present day with a segment removed for cases (a) *B0.00*, (b) *B0.22*, (c) *B0.33*, (d) *B0.44*, (e) *B0.55*, (f) *B0.66*, (g) *B0.77*, (h) *B0.88*, (i) *noU*, (j) *noCont*, (k) *U2C*, (l) *UH*. Contoured volume shows C > 0.9 material (i.e., basalt rich) excluding the uppermost 120 km.

generally slightly higher than this with the exception of cases *B0.77* and *B0.88*. For the CMB heat flux both the exact value and long term trend varies with buoyancy number. Between 250 and 600 Myr of model time, higher CMB heat fluxes are recorded for simulations with higher buoyancy numbers. Each case subsequently shows a peak in CMB heat flux after 1 Gyr of model time, with lower buoyancy number simulations experiencing higher peaks (Figure 3e). After this the CMB heat flux decreases for a period of time, the length of which increases with buoyancy number. For cases *B0.77* and *B0.88* there is prolonged low CMB heat flux until present day.

Strong similarities exist between the radially averaged radiogenic heating rate (Figure 3b) and radially averaged bulk composition (Figure 3d), which is expected as the melting process concentrates HPEs in OC material. This emphasizes how OC material has a tendency to heat up over time due to the relatively high concentrations of radioactive isotopes. Generally cases with higher buoyancy numbers have a higher concentration of basaltic material in the lowermost mantle and consequently a lower average C (more depleted) in the upper and mid mantle (Figure 3d). This is especially visible for cases with $B = 0.66$–0.88.

Mantle processing rates show significant variation with both time and buoyancy number (Figure 4) and while the long term trend differs from that of the surface heat flux, there are similarities in the details. For example, the processing rate is the same for all simulations for the first 700 Myr of model time (Figure 4). Additionally, the peaks in surface heat flux at 850 Myr and during the last 1 Gyr of model time are replicated in the processing rates.

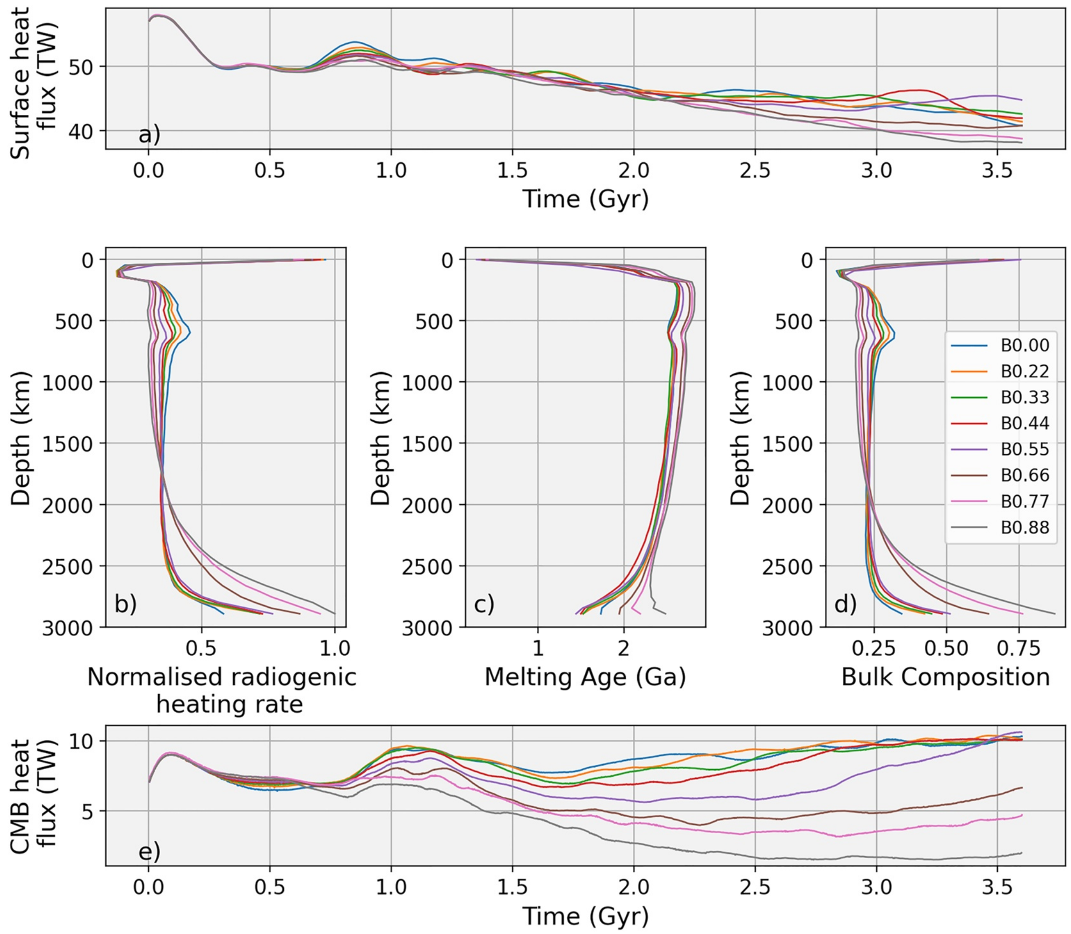

Figure 3. (a) Time varying surface heat flux, (b) radially averaged normalized radiogenic heat production, (c) radially averaged melting age (time since last melted), (d) radially averaged bulk composition, (e) time varying CMB heat flux for cases *B0.00*, *B0.22*, *B0.33*, *B0.44*, *B0.55*, *B0.66*, *B0.77*, *B0.88*. Plots b–d represent the present day state of the mantle. Legend for line color in all panels given in panel (d).

For all buoyancy numbers, histograms of the melting age (time since last melted) of particles near the CMB (Figure 5) show a peak at 0.5–0.6 Gyr after 1 Gyr of model time. This is the modal time it takes for OC material generated at the surface to descend through the mantle to the CMB. Subsequently there are strong similarities through time for simulations where the piles of subducted OC have been re-incorporated into the mantle by present day (B0.0 to *B0.55*). In these cases there is a strong skew to younger melting ages throughout the modeled time. At higher buoyancy numbers, a greater fraction of material near the CMB retains high melting ages up to the present day. The result is a bimodal distribution of present day CMB melting ages for cases with buoyancy numbers of 0.66–0.88.

Spectral heterogeneity maps of the composition field for all buoyancy numbers have power concentrated generally in 2 areas of the mantle; near the surface and the lowermost mantle (Figure 6). As buoyancy number increases from 0.0 (*B0.00*) to 0.55 (*B0.55*), there is a slight tendency for long wavelength structures (low spherical harmonic degree) to become increasingly dominant in the lower mantle and begin to extend further up into the mantle. At the same time the relatively high power signal (compared to the surrounding mantle) in the mantle transition zone tends to get weaker with increasing buoyancy number. Between cases *B0.55* and *B0.66* there is a marked change in spectral heterogeneity maps of the composition field, with significantly more power concentrated in the lower mantle large wavelength structures reaching further up into the mantle from the CMB (Figures 6e and 6f).

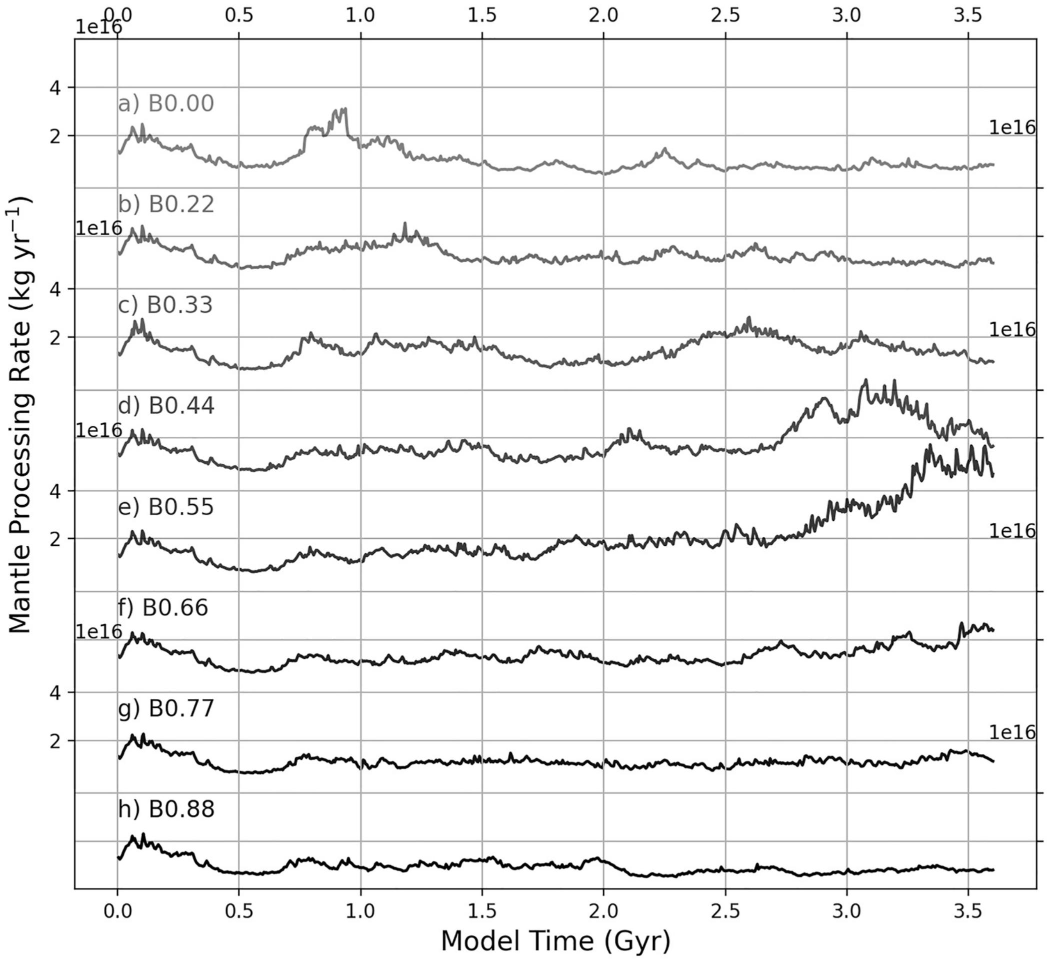

Figure 4. Melting processing rates for simulations (a) *B0.00*, (b) *B0.22*, (c) *B0.33*, (d) *B0.44*, (e) *B0.55*, (f) *B0.66*, (g) *B0.77*, (h) *B0.88*, in kg/yr. The processing rate refers to the mass of mantle that has been in a melting zone and had melt extracted.

3.2. Effects of Different Heating Conditions

Four simulations are presented in which the treatment of HPEs are modified while the buoyancy number remains fixed at the same value as case *B0.55*. Of these simulations, case *noU* shows the most similarity to case *B0.55*, almost mirroring the history of CMB coverage (Figure 1), heat flux (Figures 7a and 7e), and present day radial profiles (Figures 7b–7d). The lack of a continental reservoir in case *noCont* results in an ~30% increase in the amount of radiogenic heat production in the mantle compared to *B0.55* (Figure 7b). Consequently the surface heat flux is significantly higher than any other case with the same buoyancy number and CMB heat flux is lower due to higher mantle temperatures. The high mantle temperatures also cause more rapid remelting of material, so the melting ages throughout the mantle are younger than other cases (Figure 7c). With the exception of case *noU*, all of the cases with altered geochemical treatment result in higher peak fraction of CMB coverage and higher present day CMB coverage (Figure 1).

Case *UH*, in which radiogenic heating is uniformly distributed throughout the mantle rather than concentrated in areas enriched in HPEs, has a lower surface heat flux than case *B0.55* for the entirety of the modeled time (Figure 7a). However, the CMB heat flux is comparable for the first 2.1 Gyr of modeled time before decreasing in case *UH* relative to *B0.55* for the remaining 1.5 Gyr (Figure 7e). Case *U2C* has a slightly higher surface heat flux than *B0.55* for much of the simulation and a lower CMB heat flux for the last 2.6 Gyr, which may be understood by the greater concentration of HPEs that the mantle is initialized with.

Spectral heterogeneity maps show similar compositional structures between *noU* and *B0.55*, with little evidence of high power in low degree structures above the CMB (Figures 8a and 8b). The spectral heterogeneity maps of the

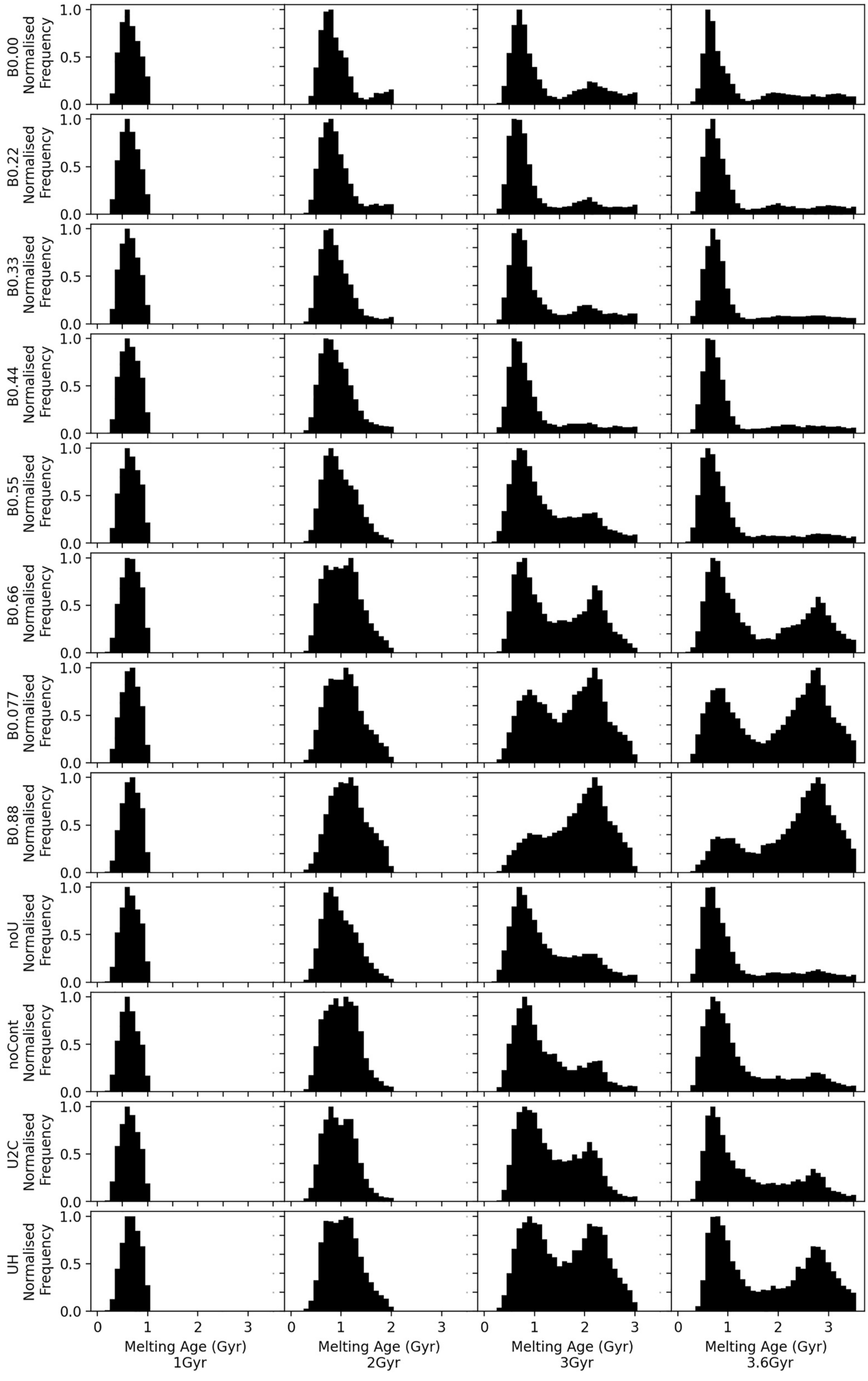

Figure 5. Histograms of the melting age (time since last melted) of enriched particles (C > 0.25) in the layer above the CMB at model times of 1, 2, 3, and 3.6 Gyr (columns left to right) for cases *B0.00*, *B0.22*, *B0.33*, *B0.44*, *B0.55*, *B0.66*, *B0.77*, *B0.88*, *noU*, *noCont*, *U2C*, *UH* (rows top to bottom). Note that particles which have not previously melted are not included.

10.1029/2022JB025610

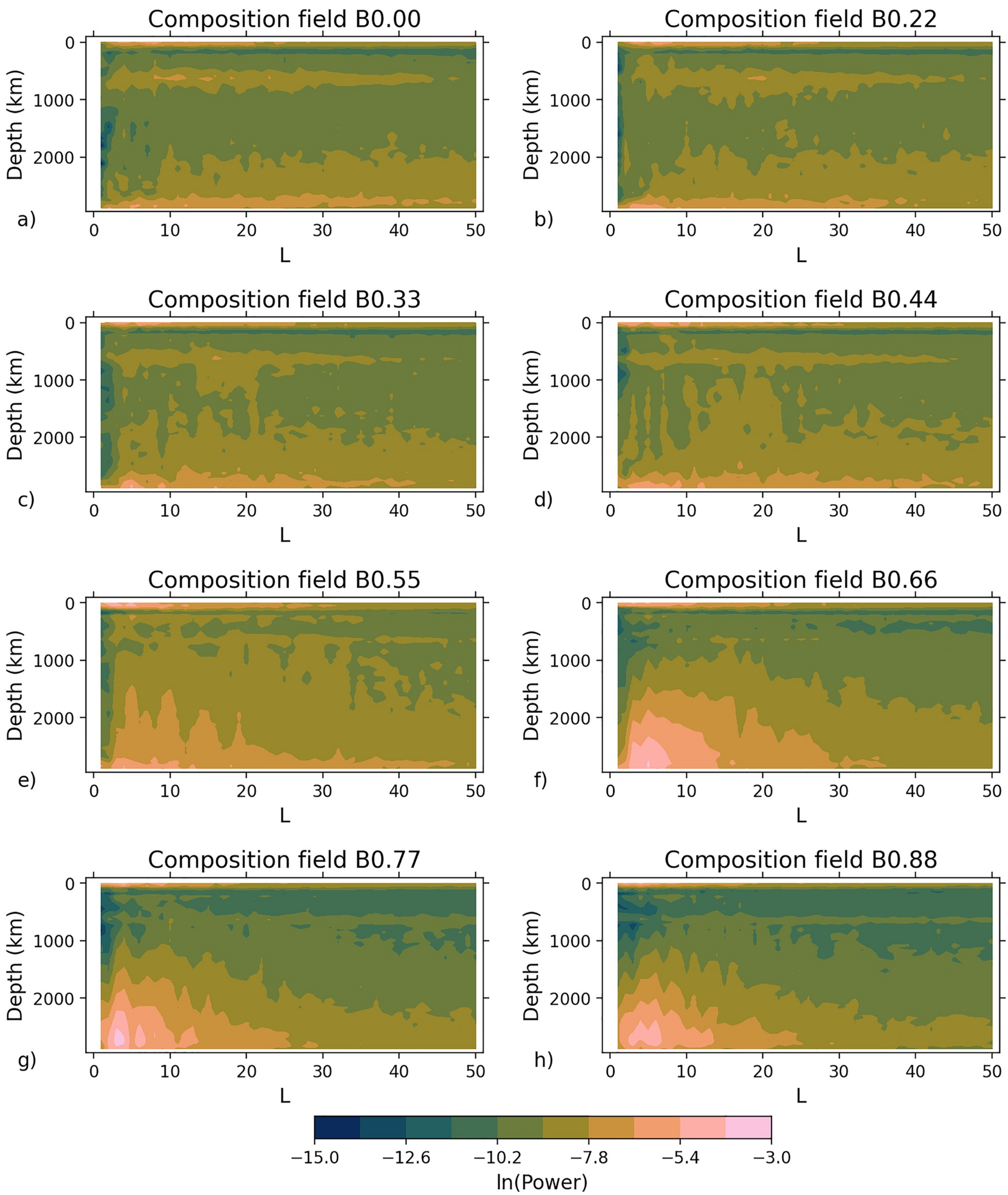

Figure 6. Spectral heterogeneity maps as a function of model depth up to spherical harmonic degree 50 of the present day bulk composition field for simulations with various buoyancy numbers.

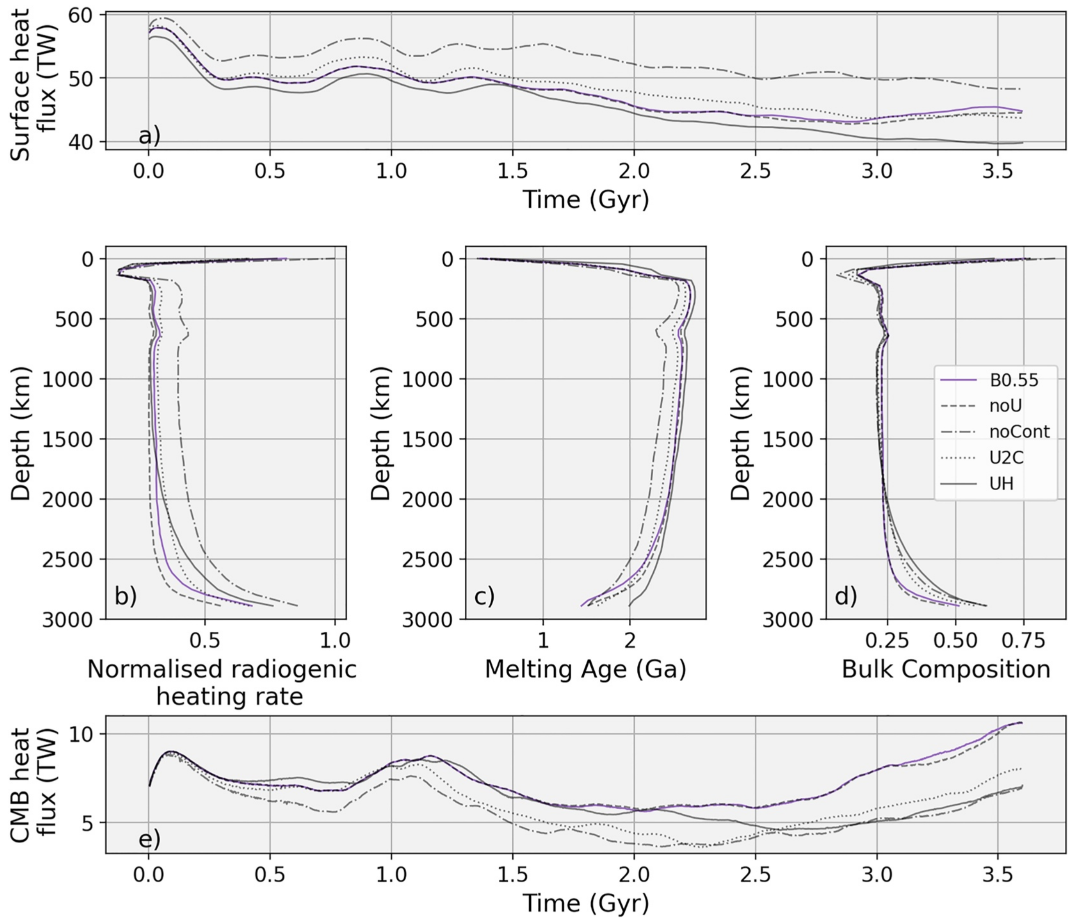

Figure 7. (a) Time varying surface heat flux, (b) radially averaged normalized radiogenic heat production, (c) radially averaged melting age (time since last melted), (d) radially averaged bulk composition, (e) time varying CMB heat flux for cases *B0.55*, *noU*, *noCont*, *U2C*, *UH*. Plots b–d represent the present day state of the mantle. Legend for line type in all panels given in panel (d).

composition field for cases *noCont*, *U2C* and *UH* show broadly similar patterns to one another(Figures 8c–8e). More power is concentrated in degree 3–8 structures in the lower mantle compared to case *B0.55*. Much like in case *B0.66*, these structures may reach up ∼600 km from the CMB. There is a bimodal distribution of melting ages in the lowermost mantle in case *UH*, similar to *B0.66* (Figure 5). For *noCont*, *U2C*, and *UH*, the distribution is more skewed toward younger melting ages, indicating that accumulations in these cases are composed of a higher fraction of more recently subducted material.

3.3. Seismic Signature

While we cannot make direct comparisons on spatial variability of seismic tomography models due to the lack of Earth-like plate geometries, we can compare against radial trends and seismic properties of piles, assuming that these correspond to LLSVPs. For case *B0.66* we present depth slices of the temperature, composition, and $\delta \ln V_s$ field at the CMB and 2,709 km depth (Figure 9). Areas where basaltic accumulations are well consolidated correspond to the pile structures observed in Figure 2f and are the hottest regions within a given layer. These regions are predicted to have a δlnV_s of ∼−1% at the CMB (Figure 9f), increasing to ∼−3% further away from the CMB (Figure 9c). The perimeters of the piles tend to be cooler and have less negative shear wave velocity anomalies. In regions where downwellings bring cooler material into the lowermost mantle (Figure 9a), faster δlnV_s are expected (Figure 9c) irrespective of the bulk composition of this material.

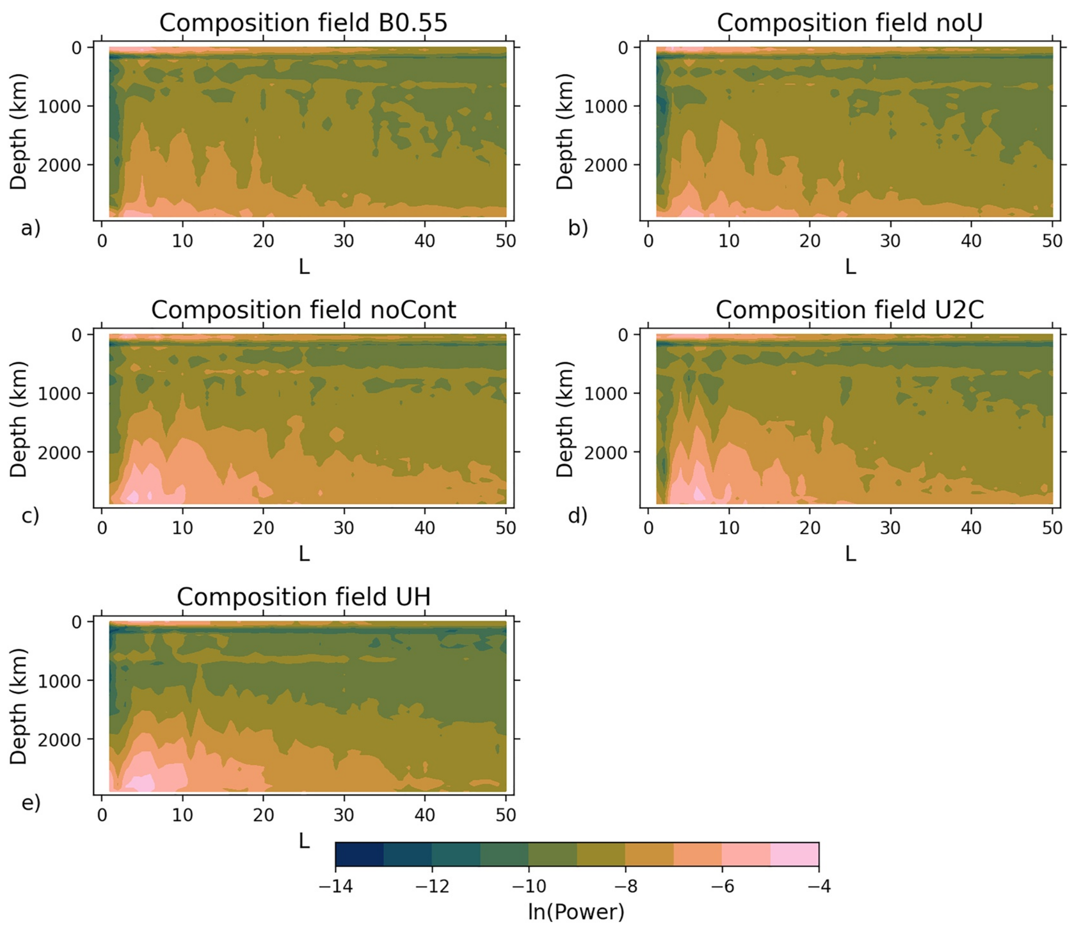

Figure 8. Spectral heterogeneity maps as a function of model depth up to spherical harmonic degree 50 of the present day bulk composition field for simulations *B0.55*, *noU*, *noCont*, *U2C*, *UH*.

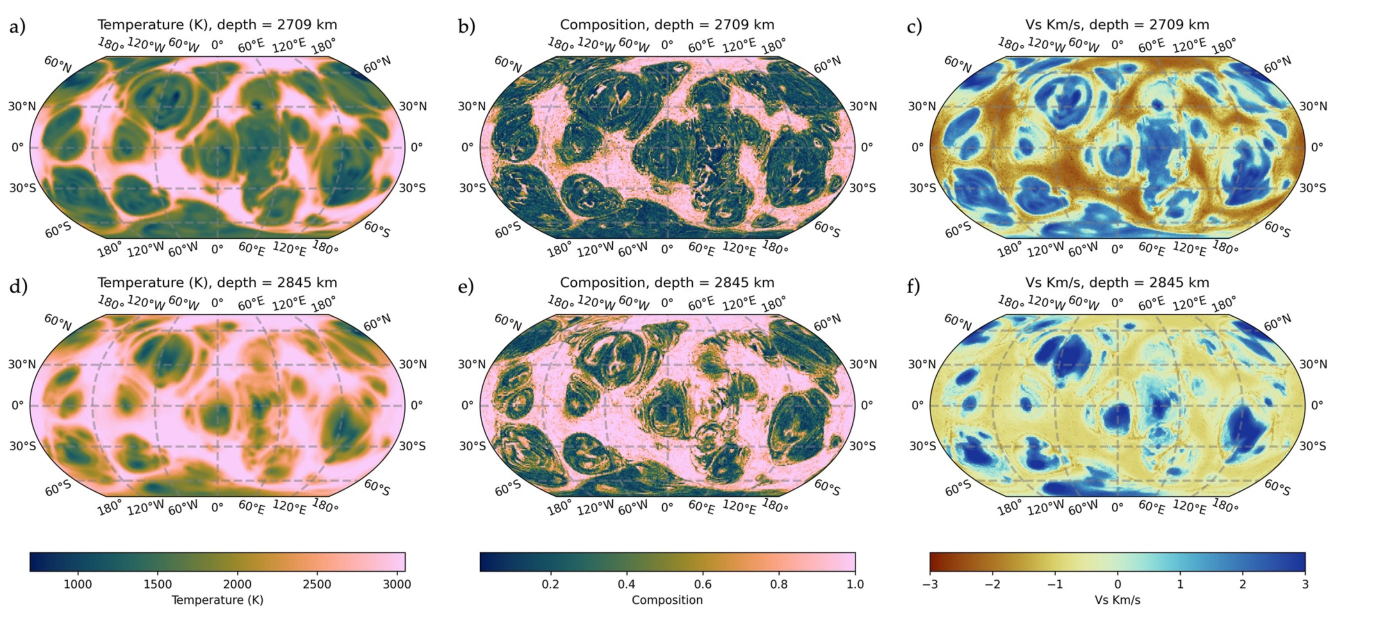

Figure 9. (a and d) Temperature, (b and e) bulk composition, and (c and f) $\delta \ln V_s$ field depth slices at a depth of 2,707 km (a–c) above the CMB (e and f) for case *B0.66*.

4. Discussion

Early in our simulations we see high melt productivity due to high internal heating rates from the decay of HPEs and consequently large volumes of OC material are subducted early on. The similarity of the surface heat flux (Figure 3a) and processing rate (Figure 4) for the first 700 Myr of the simulation indicates that the initial mantle thermal and velocity field is strongly influencing the early upper mantle dynamics. In all cases large volumes of subducted OC begin to accumulate at the CMB after around 500 Myr of model time, but depending on the buoyancy number of subducted OC in the lower mantle, we observe a range of different behaviors. For low buoyancy numbers ($B \leq 0.22$), piles do not form as subducted OC is readily mixed into the mantle.

For intermediate buoyancy numbers (*B0.33–B0.66*), we see subducted OC accumulate at the CMB at different rates, with more OC accumulating at the CMB at higher buoyancy numbers (Figure 1). The ubiquitous tendency toward more enriched compositions in the lowermost mantle (Figure 3d) shows that no matter the buoyancy number, the strength of downwellings will concentrate at least some OC material at the CMB, though its residence time will depend on the intrinsic density contrast. Only case *B0.66* retains distinct piles at the CMB to present day (Figure 2). Previous studies have also found that piles form given a sufficiently high buoyancy number (Brandenburg et al., 2008; Jones et al., 2020; Mulyukova et al., 2015), though it has been shown that the thickness of subducted OC also affects the rate of OC segregation (M. Li & McNamara, 2022). In the cases with the highest buoyancy numbers (*B0.77* and *B0.88*), the trend of more subducted OC accumulating for higher buoyancy numbers continues, but it resists being swept into distinct piles and instead forms an undulating blanket across most of the CMB (Figure 2). Similar behavior of subducted OC has previously been documented in 2D (Brandenburg et al., 2008; Mulyukova et al., 2015) and 3D (Nakagawa & Tackley, 2010) mantle convection simulations for similar buoyancy numbers ($B > 0.8$).

The longevity of subducted OC accumulations depends on the buoyancy number, which is simply explained by the greater negative chemical buoyancy imparted on the piles with increasing buoyancy number. Subducted OC is initially cool, however it heats up due to conduction from surrounding hot mantle material, from the core and from internal heating due to the decay of HPEs. This heating makes it easier to be buoyantly removed from the D" layer or entrained into upwellings. For higher buoyancy numbers, a greater thermal buoyancy is required in order to overcome the intrinsic chemical density of subducted OC and therefore it takes longer for accumulations to be entrained into the mantle (Figures 1 and 3e). As in Mulyukova et al. (2015) we see dense accumulations have an insulating effect, reducing the heat flux across the CMB (Figure 3e) and ultimately lowering the mean temperature of the mantle system.

In cases *B0.33*, *B0.44* and *B0.55* we also see periods of increased melting before the present day, peaking at 2.6, 3.1, and 3.5 Gyr of model time respectively (Figures 4c–4e), which correspond to peaks in the surface heat flux (Figure 3a). Coupled with visualizations (Supplementary videos V3–V5, https://doi.org/10.5281/zenodo.7544389), the increased melting rate and surface heat flux captures a behavior in which large volumes of pile material become positively buoyant over a relatively short space of time, resulting in them moving away from the D" layer and being sampled by melting. These large volumes correspond to ancient heterogeneity, generated due to high early melting rates. The increased melting due to this destabilization of subducted OC accumulations is more intense with increasing buoyancy number (Figure 4) because more subducted OC segregates to the CMB at higher buoyancy numbers (Figure 1). There is little evidence in Earth's geological record for a process that causes such a recent and global increase in the mantle processing rate as is seen in cases *B0.44* and *B0.55* especially. Large igneous provinces (LIPs) are known records of sudden, localized increases in melt production, however evidence of these is distributed throughout at least the last 2.5 Gyr of Earth's history (Ernst, 2014). While it is true that LIP eruption events are concentrated in Earth's more recent history, this may be due to the preservation bias associated with the recycling rates of oceanic lithosphere (Ernst et al., 2005). For case *B0.66* the piles are still largely stable at present day and so there has not yet been a distinct increase in melting (Figure 4). It is reasonable to assume though that if this simulation were allowed to continue evolving, the piles in this case also would fully destabilize, causing a large pulse in melting. This brings up the question of the length of our model time relative to the Earth. As in some previous studies (Christensen & Hofmann, 1994; Xie & Tackley, 2004), our simulations are run for 3.6 Gyr, almost 1 Gyr shorter than the age of the Earth. We do this to avoid having to simulate early Earth conditions, when mantle temperatures may have been significantly higher, leading to much lower mantle viscosities. As our simulations begin producing and recycling OC material almost immediately, we implicitly assume some recycling mechanism from 3.6 Ga. It is unlikely that modern style plate tectonics existed so early in Earth's history (Hawkesworth et al., 2020), however geodynamic models support the existence of alternative early recycling regimes, such as a plutonic-squishy lid (Lourenço et al., 2020) or plume related lithospheric dripping (Gerya et al., 2015).

The absence of U recycling from the continental reservoir in case *noU* causes a decrease in the radiogenic heating rate throughout the mantle relative to case *B0.55*, which has the same buoyancy ratio (Figure 7b), however temporal and present day radial trends show little difference (Figures 7a and 7c–7e). It is evident that the amount of U recycled in *B0.55*, which is equivalent to approximately 14% of the present day U budget, does not produce enough heat to affect the thermal evolution of the mantle in any meaningful way. This is significant as it was shown in Panton et al. (2022) that such a U recycling rate, coupled with preferential removal of Pb from OC, is sufficient to reconcile the observed Pb isotope distribution in oceanic basalts.

The presence of piles at the present day for case *UH* (Figures 2k and 8e) illustrates the importance for models to include radiogenic heating that is controlled by the local concentration of HPEs. Present day CMB coverage is increased from 47% in *B0.55%*–63% in *UH* (Figure 1) and the piles are composed of both young and ancient material (Figure 5). This indicates how lower internal heating rates within the piles inhibits their erosion. The heating rate within piles is calculated to be 1.75–2.5 times greater than in the surrounding mantle in case *B0.66* (Figure S1 in Supporting Information S1). The sensitivity of pile stability to heterogenous internal heating rate suggests that some previous work in which internal heating is either not included (Mulyukova et al., 2015) or is uniformly distributed throughout the mantle (Brandenburg et al., 2008; Jones et al., 2020) may overestimate the stability of basaltic piles at the CMB. This result is similar to work in a previous studies which show primordial piles to destabilize more readily when they experience a relatively high rate of internal heating (Citron et al., 2020) and that basaltic piles are unstable under early Earth conditions where mantle temperature and internal heating rates are high (Fujita & Ogawa, 2009; Ogawa, 2014).

The differences in the lower mantle structures observed between cases *B0.55*, *B0.66* and *B0.77* suggests that there is only a narrow range of buoyancy numbers which facilitate pile retention until present day. A potentially surprising result is that more vigorous mantle convection offered by increased internal heating due to different continental crust extraction models (cases *noCont* and *U2C*) causes an increase in the present day CMB coverage relative to *B0.55* where the buoyancy number is the same. For these cases the present day CMB coverage is most similar to *B0.66* (Figure 1) and the present day basaltic accumulations are also similar (Figures 2j and 8d). In both *noCont* and *U2C* a larger proportion of the basaltic material at the CMB is young compared to *B0.66* (Figure 5), which comprises both ancient and more contemporary recycled OC. This shows that given sufficient rates of OC production and subduction, piles may be destroyed and replenished at similar rates, allowing them to exist in a quasi-steady state. Subduction flux history is therefore an important consideration for piles composed of recycled OC. The different behaviors exhibited between simulations *B0.55*, *noU*, *noCont*, and *U2C* highlights a difficulty in accurately modeling the evolution of thermo-chemical piles composed of recycled OC when radiogenic heating is considered. Poorly constrained factors, such as the onset time of plate tectonics and the history of continental crust extraction (Hawkesworth et al., 2020) affect the concentration of HPEs in the mantle over time. Consequently, this affects the longevity of piles, making it difficult to uniquely constrain parameters pertaining to their creation. Drawing on multiple lines of evidence may assist in eliminating certain scenarios.

Within the bounds of the parameters examined in this study, the range of buoyancy numbers which permit piles to persist to the present day is $B = 0.55$ to $B = 0.66$. For our incompressible simulations in which the coefficient of thermal expansion (α) is fixed at 2.5×10^{-5} K^{-1} for all depths, this corresponds to an intrinsic density difference of +3.75%-+4.5% between OC and ambient mantle material. In the compressible terrestrial mantle, thermal expansivity is expected to decrease with depth. Such conditions would yield a reduced density difference between OC and ambient mantle material for the same buoyancy number. Thermodynamic estimates of the coefficient of thermal expansion for key mantle mineral assemblages in the D" layer suggest a value of $\sim 1.2 \times 10^{-5}$ K^{-1} (Chopelas & Boehler, 1992; Stixrude & Lithgow-Bertelloni, 2011). For this value, the range of buoyancy numbers at which piles may remain stable ($B = 0.55$–0.66) corresponds to an intrinsic density difference of +1.8%-+2.1%. This lies within the range of well accepted predictions of lower mantle density differences between OC and ambient mantle compositions (Hirose et al., 2005). More recent mineral physics calculations suggest a lower mantle density difference of no more than ~2% (Tsuchiya, 2011; W. Wang et al., 2020), which still leaves subducted OC as a contender for the chemical component of thermo-chemical LLSVPs.

LLSVPs are typically thought of as degree 2 and 3 structures (Dziewonski et al., 1977; Koelemeijer et al., 2016; Ritsema et al., 2011), however the spherical harmonic power spectrum for case *B0.66* (Figure 6f) shows high power in the lowermost mantle for degree 2–8 structures. This may be a result of the lack of Earth-like plate tectonics in the simulations presented here. Three dimensional mantle circulation models which are driven by reconstructions of past plate motion have previously been shown to generate subduction zones which sweep compositionally distinct material into piles resembling LLSVPs (Bower et al., 2013; D. R. Davies et al., 2012; McNamara & Zhong, 2004; Zhang et al., 2010). However, Earth-like plate tectonics may not necessarily be required to form degree two structures. Y. Li et al. (2014) showed that given sufficiently large thermally induced viscosity contrasts, a compositionally distinct layer may be swept into degree two structures, similar to those observed in seismic tomography (Lekic et al., 2012). Our models differ from theirs in that we dynamically generate compositionally distinct material via melting at the surface, which is then brought to the lower mantle in downwellings. It is plausible that the lack of such thermal viscosity contrasts may still contribute to the lack of strong degree 2 structures in our simulations, but the lack of an Earth-like subduction history is likely the main driver of this. An additional source of mismatch between the structures in our models and the observed morphology of LLSVPs is that we have not applied a seismic resolution filter to our results, as our models are not geographically related to Earth. Typically, this would reduce the amplitude of shorter wavelength features relative to the longer wavelength features (Ritsema et al., 2007).

Besides their morphology, LLSVPs are also constrained by their characteristic seismic velocities. For case *B0.66*, the internal $\delta \ln V_s$ of piles is predicted to be −2% (Figure 9c), which is in good agreement with observations as well as other recent numerical models (Jones et al., 2020). We find $\delta \ln V_s$ to be less negative at the base of piles than in their center (Figures 9c and 9f) while seismic observations show a gradual reduction in $\delta \ln V_s$ with depth through piles (Yuan & Li, 2022). This result is partially influenced by a lower than expected mean V_s at the base of the mantle in *B0.66* of 7.17 km s^{-1} compared to 7.26 km s^{-1} in the Preliminary Earth Reference Model (PREM, Dziewonski & Anderson, 1981). The large lateral extent of the (hot) accumulations (Figure 9e) also likely contributes to the low average V_s. The composition of the piles themselves also plays a role in less negative $\delta \ln V_s$ at their base. In our simulations, the base of piles are almost purely composed of recycled OC (Figure 9e), while at shallower depths the piles are composed of a mixture of recycled OC and more depleted material (Figure 9b). Previous studies have also highlighted similar pile stratigraphy (Ballmer et al., 2016; Jones et al., 2020; Mulyukova et al., 2015) and seismological constraints favor piles which are enriched toward their base (Richards et al., 2023). Purely basaltic material is likely to only yield $\delta \ln V_s$ comparable to LLSVPs at very high temperature contrasts (Deschamps et al., 2012), while a mixture of basaltic material and more depleted compositions may more than half this requirement (Jones et al., 2020). Positive $\delta \ln V_s$ anomalies are observed in cooler, recently subducted OC (Figure 9e). This is expected due to the strong temperature dependence of V_s, however it emphasizes that if LLSVPs are composed of recycled OC, the constituent material must be old enough to have heated up sufficiently to exhibit low V_s. As discussed above, piles cases *noCont* and *U2C* are composed of a greater proportion of young material compared to *B0.66*. We find that the predicted seismic velocities of piles in *U2C* does not differ from those in *B0.66* (Figure S2 in Supporting Information S1), so despite increased rates of replenishment, the high mantle temperatures and internal heating rates are enough to heat up subducted material to the point that it does not impart a positive $\delta \ln V_s$ signature on the piles when it becomes part of them. Predicted seismic velocities of piles in *noCont* are, however, slightly lower than those in *B0.66* (Figure S3 in Supporting Information S1), owed to even more frequent replenishment than in *U2C* (Figure 7c). Anti-correlation between temperature and V_s is consistently strong ($R^2 = -0.9$) throughout the lowermost mantle in all cases, whereas the anti-correlation between bulk composition and V_s is weaker and much more variable between simulations (e.g., $R^2 = -0.58$ in *B0.66*, 0.16 in *B0.00* at 2,709 km depth). This highlights that if thermochemical LLSVPs are composed of subducted OC, a significant role that the chemical heterogeneity plays in generating an observable signature is in heating piles more rapidly than ambient mantle.

Our study has shown that the effects of radiogenic heating is an important consideration when modeling the formation of piles of subducted OC. Piles formed from such a process have the potential to exhibit LLSVP-like seismic velocities. As estimates of lower mantle mineral densities improve, the narrow range of densities within which such piles may remain stable to the present day may assist in narrowing in on the compositional nature of LLSVPs. The lack of Earth-like plate tectonics in our simulations has limited our comparison of the generated piles to LLSVPs. A difficulty that future studies may face is in running with Earth-like plate motion histories for a comparable length of time as these simulations. Piles may comprise material as old as 2–3 Gyr (*B0.66*, Figure 5),

10.1029/2022JB025610

while the longest plate motion history models extend back to just 1 Ga (Merdith et al., 2021). The use of yield stress rheology (van Heck & Tackley, 2008) to self consistently generate subduction-zone like areas may be of use in bridging this time gap. While we have not included the effects of a dense, primordial layer in our simulations, we do not refute the potential for such compositions to exist in the mantle and play a role in LLSVP formation. Studies which combine both primordial and recycled OC material (Ballmer et al., 2016; Gülcher et al., 2021; Jones et al., 2021) will also benefit from including the effects of radiogenic heating in each of the compositions (Citron et al., 2020).

It is known that if a simulation is too spatially coarse, it may not properly resolve the dynamics of pile formation and entrainment (Tackley, 2011). To this end, we conducted resolution tests for the same parameters as *B0.66* at a lower resolution (average radial grid spacing of 90.4 km) and at a higher resolution (average radial grid spacing of 22.6 km). Spectral heterogeneity plots of the bulk composition field for these tests show that the lower resolution case (Figure S4b in Supporting Information S1) fails to build up the same long wavelength structures observed in *B0.66*. In the higher resolution case (Figure S4c in Supporting Information S1) spherical harmonic degree 2–8 compositional structures exist within the lowermost 500 km of the mantle, similar to *B0.66*. This gives us confidence that the resolution of the simulations presented in this study is sufficient to resolve the dynamics of pile formation and destruction. It has also been shown that the thickness of OC influences the ability for OC to segregate and form piles in the lower mantle (M. Li & McNamara, 2022), with more segregation occurring for thicker OC. From the bulk composition on tracer particles, we calculate the average present day thickness of OC at the surface to be ∼17 and ∼14 km in our simulations with radial resolutions of 45 and 22.5 km respectively. As this is thicker than estimates for the average OC thickness on Earth, which is ∼10 km when considering oceanic plateaus and seamounts (Tonegawa et al., 2019; White et al., 1992), the buoyancy numbers which would allow piles of recycled OC to persist to present day on Earth may differ to those in our simulations. We note that in previous studies, OC thicknesses vary from ∼6 to ∼30 km (M. Li & McNamara, 2013; Ogawa, 2003, 2010; Tackley, 2011).

In the simulations presented we have considered a single radially varying mantle viscosity profile. However, mantle viscosity, especially in the lower mantle, is poorly constrained (Kaufmann & Lambeck, 2000; Mitrovica & Forte, 2004). Simulations run with the same parameters as *B0.66* but with two different viscosity profiles for the lower mantle (*visc2* and *visc3*, Figure S5 in Supporting Information S1) retain piles to present day as shown in spectral heterogeneity maps of the composition field (Figure S6 in Supporting Information S1). The distribution of melting ages within the piles is similar to that in case *B0.66*, indicating similar long term rates of segregation and entrainment. Our depth dependent viscosity law does not capture the lateral variations in viscosity which are present in the mantle due to viscosity's dependence on temperature. This may mean that piles in our simulations are more viscous and therefore more stable than they might be in a more Earth-like setting (Y. Li et al., 2014). Temperature dependent viscosity has also been shown to enhance the rate of basalt segregation, resulting in larger accumulations of OC (M. Li & McNamara, 2013; Nakagawa & Tackley, 2011), so it is not clear exactly what effect it will have on the longevity of piles. A test simulation with the same parameters as *B0.66* was conducted with a weakly temperature dependent viscosity which varies by up to an order of magnitude (Figure S5 in Supporting Information S1). The spectral heterogeneity maps of the composition field for this simulation shows long wavelength compositional structures exist to present day (Figure S6g in Supporting Information S1). Unlike case *B0.66* the present day distribution of melting ages within piles is strongly skewed toward young, recently subducted material, with just a small proportion of piles being composed of ancient material. This indicates that replenishment may become a more important process for sustaining piles when temperature dependent viscosity is considered. Compositional dependent viscosity is an additional complexity which we do not consider, but work by (Y. Li et al., 2019) suggests that its relative importance will depend on the excess density of OC. While we have approximated the viscosity reduction in the lowermost mantle due to the post-bridgmanite phase transition in our radial viscosity profiles, considering the compressibility of the mantle would allow for a more self consistent representation of such phase changes and a more accurate comparison against seismic constraints.

5. Conclusions

We have presented 3D mantle convection simulations which are heated both from the core and internally from the decay of radioactive isotopes. Coupled with a melting regime to produce OC, this creates heterogenous heating rates throughout the mantle. In line with previous studies we have found that piles form at the CMB from subducted OC given a sufficiently high buoyancy number. Our simulations indicate that there may only be a narrow range of buoyancy numbers which would allow piles of subducted OC to form and remain stable until present day, without being so dense that they become immobile and blanket most of the CMB. While the actual buoyancy number might be adjusted with future work because of current model limitations, for the simulations presented that range is $B = 0.55–0.66$. Piles generated in our models are generally shorter wavelength features than LLSVPs, probably due to a lack of Earth-like subduction geometries, and are enriched in OC at their base. The $\delta \ln V_s$ anomaly of piles compares most favorably to LLSVPs in areas that are both hot and composed of a mixture of OC and more depleted material. This requires piles to be composed of OC which is sufficiently old so that it has been heated by radiogenic heating and conduction from the core to be hotter than the surrounding mantle.

We find that it is important for geodynamic models to include radiogenic heating which is controlled by the concentration of HPEs. Failure to do so results in an overestimation of the stability of piles. In our simulations with a buoyancy number of $B = 0.55$, heterogenous heating rates reduce the longevity of piles, decreasing present day CMB coverage from 63% to 47%. The geochemical model used in such simulations can also influence pile formation and preservation as higher HPE concentrations will result in faster mantle processing rates. In cases with higher internal heating rates piles may be sustained at lower buoyancy numbers due to partial replenishment, indicating that subduction flux may be an important consideration in modeling LLSVP formation from recycled OC. However, recycling a small amount of continental U into the mantle, as is required to reproduce the measured range of Pb isotope ratios in MORBs, has negligible effect on the dynamical evolution of our simulations.

Data Availability Statement

Model output used in the analysis presented in this work are available at http://doi.org/10.17035/d.2022.0217543433. The TERRA code used in this study is not freely available as the code predates open-source licensing. As a result, we do not have the rights to release all parts of the code, however the code pieces which have been implemented for this study are available on request from the corresponding author (JP).

Acknowledgments

This research was partially funded by the NERC funded consortium, "Mantle volatiles: processes, reservoirs and fluxes" (Grant NE/M000397/1) of the Deep Volatiles Programme, the NERC large grant "Mantle Circulation Constrained (MC2): A multidisciplinary 4D Earth framework for understanding mantle upwellings" (Grant NE/T012633/1), and also by the School of Earth and Environmental Sciences, Cardiff University. Numerical calculations were undertaken at: (a) ARCHER2, the UK's national high-performance supercomputer; (b) HAWK, part of Supercomputing Wales, the national high-performance supercomputing system for Wales. Graphs were produced using the Matplotlib package (Hunter, 2007) for Python and we make use of the scientific color map, batlow, for select figures (Crameri et al., 2020). Visualizations were produced using Paraview (Ayachit, 2015). This is Cardiff EARTH CRediT Contribution 4.

References

Andersen, M. B., Elliott, T., Freymuth, H., Sims, K. W. W., Niu, Y., & Kelley, K. A. (2015). The terrestrial uranium isotope cycle. *Nature*, *517*(7534), 356–359. https://doi.org/10.1038/nature14062

Armstrong, R. L. (1968). A model for the evolution of strontium and lead isotopes in a dynamic Earth. *Reviews of Geophysics*, *6*(2), 175–199. https://doi.org/10.1029/rg006i002p00175

Ayachit, U. (2015). *The ParaView guide: A parallel visualization application*. Kitware.

Ballmer, M. D., Schumacher, L., Lekic, V., Thomas, C., & Ito, G. (2016). Compositional layering within the large low shear-wave velocity provinces in the lower mantle. *Geochemistry, Geophysics, Geosystems*, *17*(12), 5056–5077. https://doi.org/10.1002/2016gc006605

Baumgardner, J. R. (1985). Three-dimensional treatment of convective flow in the Earth's mantle. *Journal of Statistical Physics*, *39*(5–6), 501–511. https://doi.org/10.1007/bf01008348

Bower, D. J., Gurnis, M., Seton, M., Bower, D. J., Gurnis, M., & Seton, M. (2013). Lower mantle structure from paleogeographically constrained dynamic Earth models. *Geochemistry, Geophysics, Geosystems*, *14*(1), 44–63. https://doi.org/10.1029/2012gc004267

Brandenburg, J. P., Hauri, E. H., van Keken, P. E., & Ballentine, C. J. (2008). A multiple-system study of the geochemical evolution of the mantle with force-balanced plates and thermochemical effects. *Earth and Planetary Science Letters*, *276*(1–2), 1–13. https://doi.org/10.1016/j.epsl.2008.08.027

Bunge, H.-P., Richards, M. A., & Baumgardner, J. R. (1997). A sensitivity study of three-dimensional spherical mantle convection at 10^8 Rayleigh number: Effects of depth-dependent viscosity, heating mode, and an endothermic phase change. *Journal of Geophysical Research*, *102*(B6), 11991–12007. https://doi.org/10.1029/96jb03806

Chopelas, A., & Boehler, R. (1992). Thermal expansivity in the lower mantle. *Geophysical Research Letters*, *19*(19), 1983–1986. https://doi.org/10.1029/92gl02144

Christensen, U. R., & Hofmann, A. W. (1994). Segregation of subducted oceanic crust in the convecting mantle. *Journal of Geophysical Research*, *99*(B10), 19867–19884. https://doi.org/10.1029/93jb03403

Citron, R., Lourenço, D., Wilson, A., Grima, A., Wipperfurth, S., Rudolph, M., et al. (2020). Effects of heat-producing elements on the stability of deep mantle thermochemical piles. *Geochemistry, Geophysics, Geosystems*, *21*(4), e2019GC008895. https://doi.org/10.1029/2019gc008895

Coltice, N., & Ricard, Y. (1999). Geochemical observations and one layer mantle convection. *Earth and Planetary Science Letters*, *174*(1–2), 125–137. https://doi.org/10.1016/s0012-821x(99)00258-7

Connolly, J. A. D. (2009). The geodynamic equation of state: What and how. *Geochemistry, Geophysics, Geosystems*, *10*(10). https://doi.org/10.1029/2009GC002540

Cottaar, S., & Lekić, V. (2016). Morphology of seismically slow lower mantle structures. *Geophysical Journal International*, *207*(2), 1122–1136. https://doi.org/10.1093/gji/ggw324

Crameri, F., Shephard, G. E., & Heron, P. J. (2020). The misuse of colour in science communication. *Nature Communications*, *11*(1), 1–10. https://doi.org/10.1038/s41467-020-19160-7

Davies, D. R., Davies, J. H., Bollada, P. C., Hassan, O., Morgan, K., & Nithiarasu, P. (2013). A hierarchical mesh refinement technique for global 3-D spherical mantle convection modelling. *Geoscientific Model Development*, *6*(4), 1095–1107. https://doi.org/10.5194/gmd-6-1095-2013

Davies, D. R., Goes, S., Davies, J. H., Schuberth, B. S. A., Bunge, H. P., & Ritsema, J. (2012). Reconciling dynamic and seismic models of Earth's lower mantle: The dominant role of thermal heterogeneity. *Earth and Planetary Science Letters*, *353–354*, 253–269. https://doi.org/10.1016/j.epsl.2012.08.016

Davies, D. R., Goes, S., & Lau, H. C. P. (2015). Thermally dominated deep mantle LLSVPS: A review. In A. Khan & F. Deschamps (Eds.), *The Earth's heterogeneous mantle: A geophysical, geodynamical, and geochemical perspective* (pp. 441–477). Springer International Publishing. https://doi.org/10.1007/978-3-319-15627-9_14

Davies, G. F. (2002). Stirring geochemistry in mantle convection models with stiff plates and slabs. *Geochimica et Cosmochimica Acta*, *66*(17), 3125–3142. https://doi.org/10.1016/s0016-7037(02)00915-8

Davies, G. F. (2008). Episodic layering of the early mantle by the 'basalt barrier' mechanism. *Earth and Planetary Science Letters*, *275*(3–4), 382–392. https://doi.org/10.1016/j.epsl.2008.08.036

Davies, J. H., & Davies, D. R. (2010). Earth's surface heat flux. *Solid Earth*, 1, 5–24. https://doi.org/10.5194/se-1-5-2010

Deschamps, F., Cobden, L., & Tackley, P. J. (2012). The primitive nature of large low shear-wave velocity provinces. *Earth and Planetary Science Letters*, *349–350*, 198–208. https://doi.org/10.1016/j.epsl.2012.07.012

Deschamps, F., Kaminski, E., & Tackley, P. J. (2011). A deep mantle origin for the primitive signature of ocean island basalt. *Nature Geoscience*, *4*(12), 879–882. https://doi.org/10.1038/ngeo1295

Deschamps, F., & Tackley, P. J. (2009). Searching for models of thermo-chemical convection that explain probabilistic tomography. II-Influence of physical and compositional parameters. *Physics of the Earth and Planetary Interiors*, *176*(1–2), 1–18. https://doi.org/10.1016/j.pepi.2009.03.012

Deschamps, F., & Trampert, J. (2003). Mantle tomography and its relation to temperature and composition. *Physics of the Earth and Planetary Interiors*, *140*(4), 277–291. https://doi.org/10.1016/j.pepi.2003.09.004

Dziewonski, A. M., & Anderson, D. L. (1981). Preliminary reference Earth model. *Physics of the Earth and Planetary Interiors*, *25*(4), 297–356. https://doi.org/10.1016/0031-9201(81)90046-7

Dziewonski, A. M., Hager, B. H., & O'Connell, R. J. (1977). Large-scale heterogeneities in the lower mantle. *Journal of Geophysical Research*, *82*(2), 239–255. https://doi.org/10.1029/jb082i002p00239

Ernst, R. E. (2014). Introduction, definition, and general characteristics. In *Large igneous provinces* (pp. 1–39). Cambridge University Press.

Ernst, R. E., Buchan, K. L., & Campbell, I. H. (2005). Frontiers in large igneous province research. *Lithos*, *79*(3–4), 271–297. https://doi.org/10.1016/j.lithos.2004.09.004

Fujita, K., & Ogawa, M. (2009). Basaltic accumulation instability and chaotic plate motion in the earliest mantle inferred from numerical experiments. *Journal of Geophysical Research*, *114*(B10), B10402. https://doi.org/10.1029/2008JB006222

Garnero, E. J., & McNamara, A. K. (2008). Structure and dynamics of Earth's lower mantle. *Science*, *320*(5876), 626–628. https://doi.org/10.1126/science.1148028

Gerya, T. V., Stern, R. J., Baes, M., Sobolev, S. V., & Whattam, S. A. (2015). Plate tectonics on the Earth triggered by plume-induced subduction initiation. *Nature*, *527*(7577), 221–225. https://doi.org/10.1038/nature15752

Goes, S., Cammarano, F., & Hansen, U. (2004). Synthetic seismic signature of thermal mantle plumes. *Earth and Planetary Science Letters*, *218*(3), 403–419. https://doi.org/10.1016/S0012-821X(03)00680-0

Grand, S. P., van Der Hilst, R. D., & Widiyantoro, S. (1997). Global seismic tomography: A snapshot of convection in the Earth. *Geological Society of America Today*, *7*(4), 1–7.

Gülcher, A. J. P., Ballmer, M. D., & Tackley, P. J. (2021). Coupled dynamics and evolution of primordial and recycled heterogeneity in Earth's lower mantle. *Solid Earth*, *12*(9), 2087–2107. https://doi.org/10.5194/se-12-2087-2021

Hager, B. H., Clayton, R. W., Richards, M. A., Comer, R. P., & Dziewonski, A. M. (1985). Lower mantle heterogeneity, dynamic topography and the geoid. *Nature*, *313*(6003), 541–545. https://doi.org/10.1038/313541a0

Hawkesworth, C. J., Cawood, P. A., & Dhuime, B. (2020). The evolution of the continental crust and the onset of plate tectonics. *Frontiers in Earth Science*, *8*, 1–23. https://doi.org/10.3389/feart.2020.00326

He, Y., & Wen, L. (2009). Structural features and shear-velocity structure of the "Pacific Anomaly". *Journal of Geophysical Research*, *114*(B2), B02309. https://doi.org/10.1029/2008JB005814

Hirose, K., Takafuji, N., Sata, N., & Ohishi, Y. (2005). Phase transition and density of subducted MORB crust in the lower mantle. *Earth and Planetary Science Letters*, *237*(1–2), 239–251. https://doi.org/10.1016/j.epsl.2005.06.035

Huang, C., Leng, W., & Wu, Z. (2020). The continually stable subduction, iron-spin transition, and the formation of LLSVPs from subducted oceanic crust. *Journal of Geophysical Research: Solid Earth*, *125*(1), e2019JB018262. https://doi.org/10.1029/2019jb018262

Hunter, J. D. (2007). Matplotlib: A 2D graphics environment. *Computing in Science and Engineering*, *9*(3), 90–95. https://doi.org/10.1109/mcse.2007.55

Irifune, T., & Ringwood, A. E. (1993). Phase transformations in subducted oceanic crust and buoyancy relationships at depths of 600–800 km in the mantle. *Earth and Planetary Science Letters*, *117*(1–2), 101–110. https://doi.org/10.1016/0012-821x(93)90120-x

Jones, T. D., Maguire, R. R., Van Keken, P. E., Ritsema, J., & Koelemeijer, P. (2020). Subducted oceanic crust as the origin of seismically slow lower-mantle structures. *Progress in Earth and Planetary Science*, *7*(17), 17. https://doi.org/10.1186/s40645-020-00327-1

Jones, T. D., Sime, N., & van Keken, P. E. (2021). Burying Earth's primitive mantle in the slab graveyard. *Geochemistry, Geophysics, Geosystems*, *22*(3), e2020GC009396. https://doi.org/10.1029/2020gc009396

Karato, S.-I., & Karki, B. B. (2001). Origin of lateral variation of seismic wave velocities and density in the deep mantle. *Journal of Geophysical Research*, *106*(B10), 21771–21783. https://doi.org/10.1029/2001jb000214

Kaufmann, G., & Lambeck, K. (2000). Mantle dynamics, postglacial rebound and the radial viscosity profile. *Physics of the Earth and Planetary Interiors*, *121*(3), 301–324. https://doi.org/10.1016/S0031-9201(00)00174-6

Koelemeijer, P., Ritsema, J., Deuss, A., & van Heijst, H.-J. (2016). SP12RTS: A degree-12 model of shear- and compressional-wave velocity for Earth's mantle. *Geophysical Journal International*, *204*(2), 1024–1039. https://doi.org/10.1093/gji/ggv481

Koelemeijer, P., Schuberth, B. S., Davies, D. R., Deuss, A., & Ritsema, J. (2018). Constraints on the presence of post-perovskite in Earth's lowermost mantle from tomographic-geodynamic model comparisons. *Earth and Planetary Science Letters*, *494*, 226–238. https://doi.org/10.1016/j.epsl.2018.04.056

Kokfelt, T. F., Hoernle, K., Hauff, F., Fiebig, J., Werner, R., & Garbe-Schönberg, D. (2006). Combined trace element and Pb-Nd–Sr-O isotope evidence for recycled oceanic crust (upper and lower) in the Iceland mantle plume. *Journal of Petrology*, *47*(9), 1705–1749. https://doi.org/10.1093/petrology/egl025

Labrosse, S., Hernlund, J. W., & Coltice, N. (2007). A crystallizing dense magma ocean at the base of the Earth's mantle. *Nature*, *450*(7171), 866–869. https://doi.org/10.1038/nature06355

Lassiter, J. C. (2004). Role of recycled oceanic crust in the potassium and argon budget of the Earth: Toward a resolution of the "missing argon" problem. *Geochemistry, Geophysics, Geosystems*, *5*(11). https://doi.org/10.1029/2004GC000711

Le Bars, M., & Davaille, A. (2004). Whole layer convection in a heterogeneous planetary mantle. *Journal of Geophysical Research*, *109*(B3), 3403. https://doi.org/10.1029/2003jb002617

Lekic, V., Cottaar, S., Dziewonski, A., & Romanowicz, B. (2012). Cluster analysis of global lower mantle tomography: A new class of structure and implications for chemical heterogeneity. *Earth and Planetary Science Letters*, *357–358*, 68–77. https://doi.org/10.1016/j.epsl.2012.09.014

Li, M., & McNamara, A. K. (2013). The difficulty for subducted oceanic crust to accumulate at the Earth's core-mantle boundary. *Journal of Geophysical Research: Solid Earth*, *118*(4), 1807–1816. https://doi.org/10.1002/jgrb.50156

Li, M., & McNamara, A. K. (2018). The influence of deep mantle compositional heterogeneity on Earth's thermal evolution. *Earth and Planetary Science Letters*, *500*, 86–96. https://doi.org/10.1016/j.epsl.2018.08.009

Li, M., & McNamara, A. K. (2022). Evolving morphology of crustal accumulations in Earth's lowermost mantle. *Earth and Planetary Science Letters*, *577*, 117265. https://doi.org/10.1016/j.epsl.2021.117265

Li, Y., Deschamps, F., & Tackley, P. J. (2014). The stability and structure of primordial reservoirs in the lower mantle: Insights from models of thermochemical convection in three-dimensional spherical geometry. *Geophysical Journal International*, *199*(2), 914–930. https://doi.org/10.1093/gji/ggu295

Li, Y., Deschamps, F., Yang, J., Chen, L., Zhao, L., & Tackley, P. J. (2019). Effects of the compositional viscosity ratio on the long-term evolution of thermochemical reservoirs in the deep mantle. *Geophysical Research Letters*, *46*(16), 9591–9601. https://doi.org/10.1029/2019gl083668

Lourenço, D. L., Rozel, A. B., Ballmer, M. D., & Tackley, P. J. (2020). Plutonic-squishy lid: A new global tectonic regime generated by intrusive magmatism on Earth-like planets. *Geochemistry, Geophysics, Geosystems*, *21*(4), e2019GC008756. https://doi.org/10.1029/2019gc008756

Maguire, R., Ritsema, J., van Keken, P. E., Fichtner, A., & Goes, S. (2016). P- and S-wave delays caused by thermal plumes. *Geophysical Journal International*, *206*(2), 1169–1178. https://doi.org/10.1093/gji/ggw187

Masters, G., Laske, G., Bolton, H., & Dziewonski, A. (2000). The relative behavior of shear velocity, bulk sound speed, and compressional velocity in the mantle: Implications for chemical and thermal structure. *Geophysical Monograph Series*, *117*, 63–87.

Matas, J., & Bukowinski, M. S. (2007). On the anelastic contribution to the temperature dependence of lower mantle seismic velocities. *Earth and Planetary Science Letters*, *259*(1), 51–65. https://doi.org/10.1016/j.epsl.2007.04.028

McKenzie, D. P., Roberts, J. M., & Weiss, N. O. (1974). Convection in the Earth's mantle: Towards a numerical simulation. *Journal of Fluid Mechanics*, *62*(3), 465–538. https://doi.org/10.1017/s0022112074000784

McNamara, A. K., & Zhong, S. (2004). Thermochemical structures within a spherical mantle: Superplumes or piles? *Journal of Geophysical Research*, *109*(7), 1–14. https://doi.org/10.1029/2003jb002847

Merdith, A. S., Williams, S. E., Collins, A. S., Tetley, M. G., Mulder, J. A., Blades, M. L., et al. (2021). Extending full-plate tectonic models into deep time: Linking the Neoproterozoic and the Phanerozoic. *Earth-Science Reviews*, *214*, 103477. https://doi.org/10.1016/j.earscirev.2020.103477

Michard, A., & Albarede, F. (1985). Hydrothermal uranium uptake at ridge crests. *Nature*, *313*(6003), 47–48. https://doi.org/10.1038/317244a0

Mitrovica, J., & Forte, A. (2004). A new inference of mantle viscosity based upon joint inversion of convection and glacial isostatic adjustment data. *Earth and Planetary Science Letters*, *225*(1), 177–189. https://doi.org/10.1016/j.epsl.2004.06.005

Mulyukova, E., Steinberger, B., Dabrowski, M., & Sobolev, S. V. (2015). Survival of LLSVPs for billions of years in a vigorously convecting mantle: Replenishment and destruction of chemical anomaly. *Journal of Geophysical Research: Solid Earth*, *120*(5), 3824–3847. https://doi.org/10.1002/2014jb011688

Nakagawa, T., & Tackley, P. J. (2010). Influence of initial CMB temperature and other parameters on the thermal evolution of Earth's core resulting from thermochemical spherical mantle convection. *Geochemistry, Geophysics, Geosystems*, *11*(6), 6001. https://doi.org/10.1029/2010gc003031

Nakagawa, T., & Tackley, P. J. (2011). Effects of low-viscosity post-perovskite on thermo-chemical mantle convection in a 3-d spherical shell. *Geophysical Research Letters*, *38*(4), L04309. https://doi.org/10.1029/2010GL046494

Nakagawa, T., & Tackley, P. J. (2014). Influence of combined primordial layering and recycled MORB on the coupled evolution of Earth's mantle and core. *Geochemistry, Geophysics, Geosystems*, *15*, 4692–4711. https://doi.org/10.1002/2013GC005128

Ni, S., Tan, E., Gurnis, M., & Helmberger, D. (2002). Sharp sides to the African superplume. *Science*, *296*(5574), 1850–1852. https://doi.org/10.1126/science.1070698

Ogawa, M. (2003). Chemical stratification in a two-dimensional convecting mantle with magmatism and moving plates. *Journal of Geophysical Research*, *108*(B12), 2561. https://doi.org/10.1029/2002JB002205

Ogawa, M. (2007). Superplumes, plates, and mantle magmatism in two-dimensional numerical models. *Journal of Geophysical Research*, *112*(B6), B06404. https://doi.org/10.1029/2006JB004533

Ogawa, M. (2010). Variety of plumes and the fate of subducted basaltic crusts. *Physics of the Earth and Planetary Interiors*, *183*(1), 366–375. (Special Issue on Deep Slab and Mantle Dynamics). https://doi.org/10.1016/j.pepi.2010.05.001

Ogawa, M. (2014). Two-stage evolution of the Earth's mantle inferred from numerical simulation of coupled magmatism-mantle convection system with tectonic plates. *Journal of Geophysical Research: Solid Earth*, *119*(3), 2462–2486. https://doi.org/10.1002/2013JB010315

Oldham, D., & Davies, J. H. (2004). Numerical investigation of layered convection in a three-dimensional shell with application to planetary mantles. *Geochemistry, Geophysics, Geosystems*, *5*(12), Q12C04. https://doi.org/10.1029/2003gc000603

Ono, S., Ito, E., & Katsura, T. (2001). Mineralogy of subducted basaltic crust (MORB) from 25 to 37 GPa, and chemical heterogeneity of the lower mantle. *Earth and Planetary Science Letters*, *190*(1), 57–63. https://doi.org/10.1016/s0012-821x(01)00375-2

Panton, J., Davies, J. H., Elliott, T., Andersen, M., Porcelli, D., & Price, M. G. (2022). Investigating influences on the Pb Pseudo-Isochron using three-dimensional mantle convection models with a continental reservoir. *Geochemistry, Geophysics, Geosystems*, *23*(8), e2021GC010309. https://doi.org/10.1029/2021GC010309

Price, M., Davies, J., & Panton, J. (2019). Controls on the deep-water cycle within three-dimensional mantle convection models. *Geochemistry, Geophysics, Geosystems*, *20*(5). https://doi.org/10.1029/2018gc008158

Richards, F. D., Hoggard, M. J., Ghelichkhan, S., Koelemeijer, P., & Lau, H. C. (2023). Geodynamic, geodetic, and seismic constraints favour deflated and dense-cored LLVPs. *Earth and Planetary Science Letters*, *602*, 117964. https://doi.org/10.1016/j.epsl.2022.117964

Ricolleau, A., Perrillat, J.-P., Fiquet, G., Daniel, I., Matas, J., Addad, A., et al. (2010). Phase relations and equation of state of a natural MORB: Implications for the density profile of subducted oceanic crust in the Earth's lower mantle. *Journal of Geophysical Research*, *115*(B8), 8202. https://doi.org/10.1029/2009jb006709

Ringwood, A. E., & Irifune, T. (1988). Nature of the 650–km seismic discontinuity: Implications for mantle dynamics and differentiation. *Nature*, *331*(6152), 131–136. https://doi.org/10.1038/331131a0

Ritsema, J., Deuss, A., Van Heijst, H. J., & Woodhouse, J. H. (2011). S40RTS: A degree-40 shear-velocity model for the mantle from new Rayleigh wave dispersion, teleseismic traveltime and normal-mode splitting function measurements. *Geophysical Journal International*, *184*(3), 1223–1236. https://doi.org/10.1111/j.1365-246x.2010.04884.x

Ritsema, J., McNamara, A. K., & Bull, A. L. (2007). Tomographic filtering of geodynamic models: Implications for models interpretation and large-scale mantle structure. *Journal of Geophysical Research*, *112*(1), B01303. https://doi.org/10.1029/2006jb004566

Romanowicz, B. (2001). Can we resolve 3D density heterogeneity in the lower mantle? *Geophysical Research Letters*, *28*(6), 1107–1110. https://doi.org/10.1029/2000gl012278

Schubert, G., Masters, G., Olson, P., & Tackley, P. (2004). Superplumes or plume clusters? *Physics of the Earth and Planetary Interiors*, *146*(1–2), 147–162. https://doi.org/10.1016/j.pepi.2003.09.025

Sobolev, A. V., Hofmann, A. W., & Nikogosian, I. K. (2000). Recycled oceanic crust observed in 'ghost plagioclase' within the source of Mauna Loa lavas. *Nature*, *404*(6781), 986–990. https://doi.org/10.1038/35010098

Stixrude, L., & Lithgow-Bertelloni, C. (2011). Thermodynamics of mantle minerals - II. Phase equilibria. *Geophysical Journal International*, *184*(3), 1180–1213. https://doi.org/10.1111/j.1365-246x.2010.04890.x

Stixrude, L., & Lithgow-Bertelloni, C. (2022). Thermal expansivity, heat capacity and bulk modulus of the mantle. *Geophysical Journal International*, *228*(2), 1119–1149. https://doi.org/10.1093/gji/ggab394

Tackley, P. J. (2011). Living dead slabs in 3-D: The dynamics of compositionally-stratified slabs entering a "slab graveyard" above the core-mantle boundary. *Physics of the Earth and Planetary Interiors*, *188*(3–4), 150–162. https://doi.org/10.1016/j.pepi.2011.04.013

Tackley, P. J. (2012). Dynamics and evolution of the deep mantle resulting from thermal, chemical, phase and melting effects. *Earth-Science Reviews*, *110*(1–4), 1–25. https://doi.org/10.1016/j.earscirev.2011.10.001

Tatsumi, Y., & Kogiso, T. (1997). Trace element transport during dehydration processes in the subducted oceanic crust: 2. Origin of chemical and physical characteristics in arc magmatism. *Earth and Planetary Science Letters*, *148*(1), 207–221. https://doi.org/10.1016/S0012-821X(97)00019-8

Thorne, M. S., Garnero, E. J., & Grand, S. P. (2004). Geographic correlation between hot spots and deep mantle lateral shear-wave velocity gradients. *Physics of the Earth and Planetary Interiors*, *146*(1), 47–63. https://doi.org/10.1016/j.pepi.2003.09.026

Tonegawa, T., Miura, S., Ishikawa, A., Sano, T., Suetsugu, D., Isse, T., et al. (2019). Characterization of crustal and uppermost-mantle seismic discontinuities in the Ontong Java Plateau. *Journal of Geophysical Research: Solid Earth*, *124*(7), 7155–7170. https://doi.org/10.1029/2018JB016970

Tsuchiya, T. (2011). Elasticity of subducted basaltic crust at the lower mantle pressures: Insights on the nature of deep mantle heterogeneity. *Physics of the Earth and Planetary Interiors*, *188*(3–4), 142–149. https://doi.org/10.1016/j.pepi.2011.06.018

Turcotte, D. L. (1980). On the thermal evolution of the Earth. *Earth and Planetary Science Letters*, *48*(1), 53–58. https://doi.org/10.1016/0012-821x(80)90169-7

van Heck, H. J., Davies, J. H., Elliott, T., & Porcelli, D. (2016). Global-scale modelling of melting and isotopic evolution of Earth's mantle: Melting modules for TERRA. *Geoscientific Model Development*, *9*(4), 1399–1411. https://doi.org/10.5194/gmd-9-1399-2016

van Heck, H. J., & Tackley, P. J. (2008). Planforms of self-consistently generated plates in 3D spherical geometry. *Geophysical Research Letters*, *35*(19), L19312. https://doi.org/10.1029/2008gl035190

van Keken, P. E., & Ballentine, C. J. (1998). Whole-mantle versus layered mantle convection and the role of a high-viscosity lower mantle in terrestrial volatile evolution. *Earth and Planetary Science Letters*, *156*(1–2), 19–32. https://doi.org/10.1016/s0012-821x(98)00023-5

Wang, W., Xu, Y., Sun, D., Ni, S., Wentzcovitch, R., & Wu, Z. (2020). Velocity and density characteristics of subducted oceanic crust and the origin of lower-mantle heterogeneities. *Nature Communications*, *11*(1), 1–8. https://doi.org/10.1038/s41467-019-13720-2

Wang, X.-J., Chen, L.-H., Hofmann, A. W., Hanyu, T., Kawabata, H., Zhong, Y., et al. (2018). Recycled ancient ghost carbonate in the Pitcairn mantle plume. *Proceedings of the National Academy of Sciences*, *115*(35), 8682–8687. https://doi.org/10.1073/pnas.1719570115

White, R. S., McKenzie, D., & O'Nions, R. K. (1992). Oceanic crustal thickness from seismic measurements and rare earth element inversions. *Journal of Geophysical Research*, *97*(B13), 19683–19715. https://doi.org/10.1029/92JB01749

Williams, C. D., Li, M., McNamara, A. K., Garnero, E. J., & Van Soest, M. C. (2015). Episodic entrainment of deep primordial mantle material into ocean island basalts. *Nature Communications*, *6*(1), 1–7. https://doi.org/10.1038/ncomms9937

Wolstencroft, M., & Davies, J. H. (2011). Influence of the Ringwoodite-Perovskite transition on mantle convection in spherical geometry as a function of Clapeyron slope and Rayleigh number. *Solid Earth*, *2*(2), 315–326. https://doi.org/10.5194/se-2-315-2011

Xie, S., & Tackley, P. J. (2004). Evolution of U-Pb and Sm-Nd systems in numerical models of mantle convection and plate tectonics. *Journal of Geophysical Research B: Solid Earth*, *109*(11), 1–22. https://doi.org/10.1029/2004jb003176

Xu, W., Lithgow-Bertelloni, C., Stixrude, L., & Ritsema, J. (2008). The effect of bulk composition and temperature on mantle seismic structure. *Earth and Planetary Science Letters*, *275*(1–2), 70–79. https://doi.org/10.1016/j.epsl.2008.08.012

Yuan, Q., & Li, M. (2022). Instability of the African large low-shear-wave-velocity province due to its low intrinsic density. *Nature Geoscience*, *2022*(4), 1–6. https://doi.org/10.1038/s41561-022-00908-3

Zhang, N., Zhong, S., Leng, W., & Li, Z. X. (2010). A model for the evolution of the Earth's mantle structure since the Early Paleozoic. *Journal of Geophysical Research*, *115*(B6), 6401. https://doi.org/10.1029/2009jb006896